Materials & Design 224 (2022) 111368

Contents lists available at ScienceDirect

Materials & Design

journal homepage: www.elsevier.com/locate/matdes

Thermodynamics, microstructure evolution and mechanical properties of Al- and C-added CoFeMnNi multi-principal element alloys

Fabian Kies [a,*], Mehdi Noori [b], Simon Ewald [c], Johannes H. Schleifenbaum [c], Bengt Hallstedt [b], Christian Haase [a]

[a] Steel Institute, RWTH Aachen University, Intzestr. 1, 52072 Aachen, Germany
[b] Materials Applications in Mechanical Engineering, RWTH Aachen University, Augustinerbach 4, 52062 Aachen, Germany
[c] Digital Additive Production, RWTH Aachen University, Campus-Boulevard 73, 52074 Aachen, Germany

HIGHLIGHTS

- CoFeMnNi is FCC with low strength and ductility, where TWIP is suppressed by high SFE.
- High C solid solution hardening was observed and C–Mn clusters caused TWIP activation.
- Plate- and island-shaped $B2_{NiAl}$ formed by Al addition, which led to embrittlement.
- Combined Al and C in FCC CoFeMnNi resulted in additional TWIP activation.

GRAPHICAL ABSTRACT

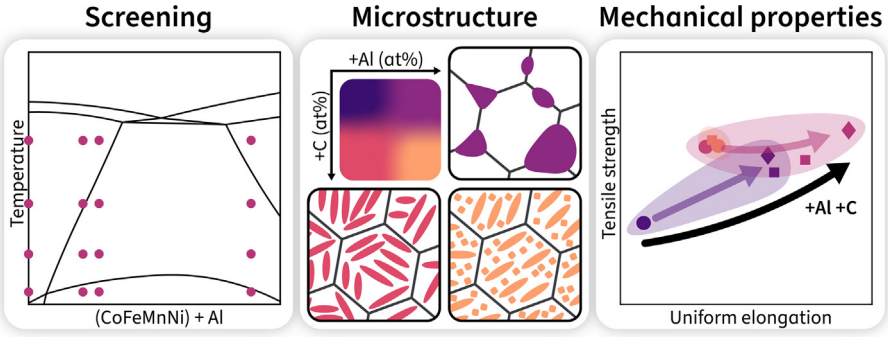

ARTICLE INFO

Article history:
Received 27 September 2022
Revised 31 October 2022
Accepted 9 November 2022
Available online 19 November 2022

Keywords:
CALPHAD
Additive manufacturing
Microstructure formation mechanism
Atomic ordering
Deformation twinning
High-entropy alloy

ABSTRACT

Navigating through the phase space of multi-principal element alloys (MPEAS) with desired microstructures and outstanding properties is challenging due to extremely high degrees of freedom in alloy composition and processing conditions. Separate Al and C additions and the resulting precipitation of hard phases are commonly used to strengthen CoCrFeMnNi-type alloys. However, the combined alloying effect and especially the high hardening potential of C in solid solution of MPEAS are rarely investigated, but the few existing investigations reveal a high potential. Therefore, the properties of the $Al_{0-22.1}C_{0-2.3}(CoFeMnNi)_{100-75.6}$ (at.%) system were comprehensively investigated, where Cr was intentionally removed to keep C in solid solution. For theoretical and experimental screening of the system, a custom CALPHAD database was extended, samples were manufactured by additive manufacturing (AM) and annealed between temperatures of 1150 and 550 °C. Detailed microstructural and mechanical analysis on 40 different revealed the properties of the equiatomic CoFeMnNi alloy and the effect of the separate and combined additions of Al and C, including comprehensive precipitate characterization. The system was especially potent in its room temperature tensile properties in the Al- and C-added FCC-based region, where it caused the activation of twinning-induced plasticity (TWIP) and combined high strength and ductility increases.

* Corresponding author.
E-mail address: fabian.kies@iehk.rwth-aachen.de (F. Kies).

https://doi.org/10.1016/j.matdes.2022.111368
0264-1275/

1. Introduction

Multi-principal element alloys (MPEAs) are still a comparatively young class of metallic materials, which are characterized by an alloy design strategy that comprises multiple major elements [1–3]. The terms high-entropy alloy (HEA) and compositionally-complex alloy (CCA) are often used for single-phase and multi-phase alloys, respectively, for which MPEA is the umbrella term [3]. MPEA design strategies are in strong contrast to established alloys that are defined by one major base element, e.g., Fe in steel, and additions of minor elements to tailor the microstructure and properties, e.g., C in steel. Some MPEAs have shown promising properties, such as high strength and hardness, high corrosion resistance, excellent wear resistance, and good thermal stability [4–10], but industrial adoption is still low. Within MPEAs, the single-phase face-centered cubic (FCC) CoCrFeMnNi Cantor alloy [1] is the most frequently investigated alloy [3]. As with other single-phase MPEAs, its strength at room temperature is low compared to conventional alloys [4,11].

The addition of certain elements has a strong impact on the developing microstructure and can therefore be used to tailor the properties of MPEAs [7,12–21]. Most commonly, Al is used in Cantor-type alloys to stabilize the ordered body-centered cubic (BCC) phase $B2_{NiAl}$ to increase yield strength and hardness [22,2,23,13,16,24–32] simultaneous to a density reduction [2]. However, high volume fractions of $B2_{NiAl}$ lead to undesirable embrittlement [23]. Other methods to increase strength are interstitial alloying elements such as C [33–35], N [33,36,37,34,38,39] and B [40], which increase strength effectively even at low contents. Especially the addition of C is interesting as it is extensively and effectively used for strengthening in FCC-based alloys, both for precipitation [41] and solid solution hardening [42]. The effect of C addition in Cantor-type alloys is already well researched [43,14,44–54]. Increased C contents lead to carbide precipitation, which increases strength and results in a grain refining effect by pinning grain boundaries during annealing. However, combined with high Cr contents, the formation of $M_{23}C_6$-type carbides was often observed, resulting in embrittlement [14]. The effect of extensive solid solution hardening by C was rarely investigated in MPEAs [55,56], but a much higher hardening potential compared to conventional alloys [57] was observed.

In this work, we aim to combine the effects of Al and C alloying in Cantor-type MPEAs to tailor the microstructure and resulting mechanical properties. To increase solubility of C in the FCC phase, Cr was removed from the CoCrFeMnNi composition due to its high affinity to form $M_{23}C_6$-type carbides. In a previous study [58], Al and C additions to CoFeMnNi led to enhanced strength without the loss of ductility due to a modification of the stacking-fault energy (SFE). However, aging treatments leading to precipitation strengthening were not investigated further, but already revealed a high potential for strengthening [59].

To screen and identify promising chemical compositions and heat treatment windows, thermodynamic calculations using the calculation of phase diagrams (CALPHAD) method [60,61] have been proven to be a powerful method to guide the design of new MPEAs [62–65]. Previously, a custom CALPHAD database for MPEAs was developed by the authors for the CoCrFeMnNi system [66]. The database was extended to also contain Al and C, which already resulted in reasonable phase predictions in AlCCoCrFeMnNi systems [58,59] and was applied in the present study.

To investigate the properties of Al- and C-added CoFeMnNi alloys in detail, an approach combining thermodynamic calculations with additive manufacturing (AM) was used to allow for high-throughput theoretical and experimental screening, as described by Haase et al. [66] and applied previously in [58]. For thermodynamic calculations, the custom CoCrFeMnNi CALPHAD database was fully extended by Al and C. Samples with desired compositions were manufactured by laser beam powder bed fusion (PBF-LB) using powder blends as input to vary the chemical composition [67]. After heat treatments, the microstructure and mechanical properties were evaluated. The accuracy of the thermodynamic calculations was compared to the obtained microstructures and the resulting mechanical properties. The boundaries of C solution in the FCC matrix and precipitate types with increased Al- and C content were investigated in detail to give an overview of the properties in $Al_xC_y(CoFeMnNi)_{100-x-y}$ alloys. The occurring microstructure formation and strengthening mechanisms are discussed and correlated with the resulting mechanical properties.

2. Applied methods

2.1. Thermodynamic calculations

Thermodynamic calculations using the CALPHAD method [60,61] were used to select appropriate alloy compositions for production and characterization. The database previously constructed for the Cantor system (CoCrFeMnNi) by Haase et al. [66] was extended by Al and C. Further information on the extension of the database can be found in the supplementary material.

Mappings with the equiatomic CoFeMnNi composition as function of Al at fixed C contents were made to identify suitable compositions. Cr was excluded from the commonly used Cantor alloy system [3,4] to increase C solubility in the FCC phase and decrease the temperature for carbide precipitation. The CoFeMnNi-base alloys are denoted as Al^xC^y in this work, with x and y representing the atomic fraction of Al and C, respectively. The target compositions identified (Fig. 1) were $Al^{0.0,\ 6.0,\ 8.0,\ 22.0}C^{0.0,\ 1.4,\ 2.8}$ for the FCC → (FCC + B2) and (FCC + B2) → B2 transitions. The Thermo-Calc software was used for all the CALPHAD calculations [68].

2.2. Material and processing

An Aconity*MINI* PBF-LB machine by Aconity3D with different elemental powder blends as input material was used to manufacture specimens, where fully dense and compositionally homogeneous samples without processing defects were obtained (see Ewald et al. [67] for a detailed analysis). Depending on the initial powder mixture, fully dense 5 × 5 × 10 mm^3 specimens were manufactured with 120 to 200 W laser power, 350 to 650 mm s^{-1} scanning speed, 60 to 90 µm hatch distance and 30 µm layer thickness. Samples with the powder mixtures $Al^{22.0}C^{1.4,\ 2.8}$ could not be manufactured due to a tendency to form cracks during the process. The as-built $Al^xC^{0.0}$, $Al^xC^{1.4}$ and $Al^xC^{2.8}$ samples were subsequently homogenized for 3 h at 1150, 1100 and 1050 °C, respectively. Afterward, annealing was performed at 550, 700 and 900 °C for 24 h. Heat treatments were performed in a Thermconcept muffle furnace with subsequent water quenching, where the samples were wrapped in Knu-foil to prevent oxidation. The wet chemical analysis in the as-built condition is shown in Table 1 and the Al^xC^y alloys will be referenced by their measured chemical composition.

The typical features of the AM microstructure are elongated grains in build-up direction, strong texturing, elemental segregation, high dislocation density [69] and oxide formation [67,70]. As the materials properties were the focus of the study, all investigated samples were first homogenized at high temperatures (1050 to 1150 °C), which resulted in recrystallization. Consequently, the AM microstructural features were removed [71,72]. The material still contained small amounts of Mn or Al oxides, which were introduced by the elemental powder's high affinity to oxygen [67,70] and also resulted in the formation of micropores. These oxides

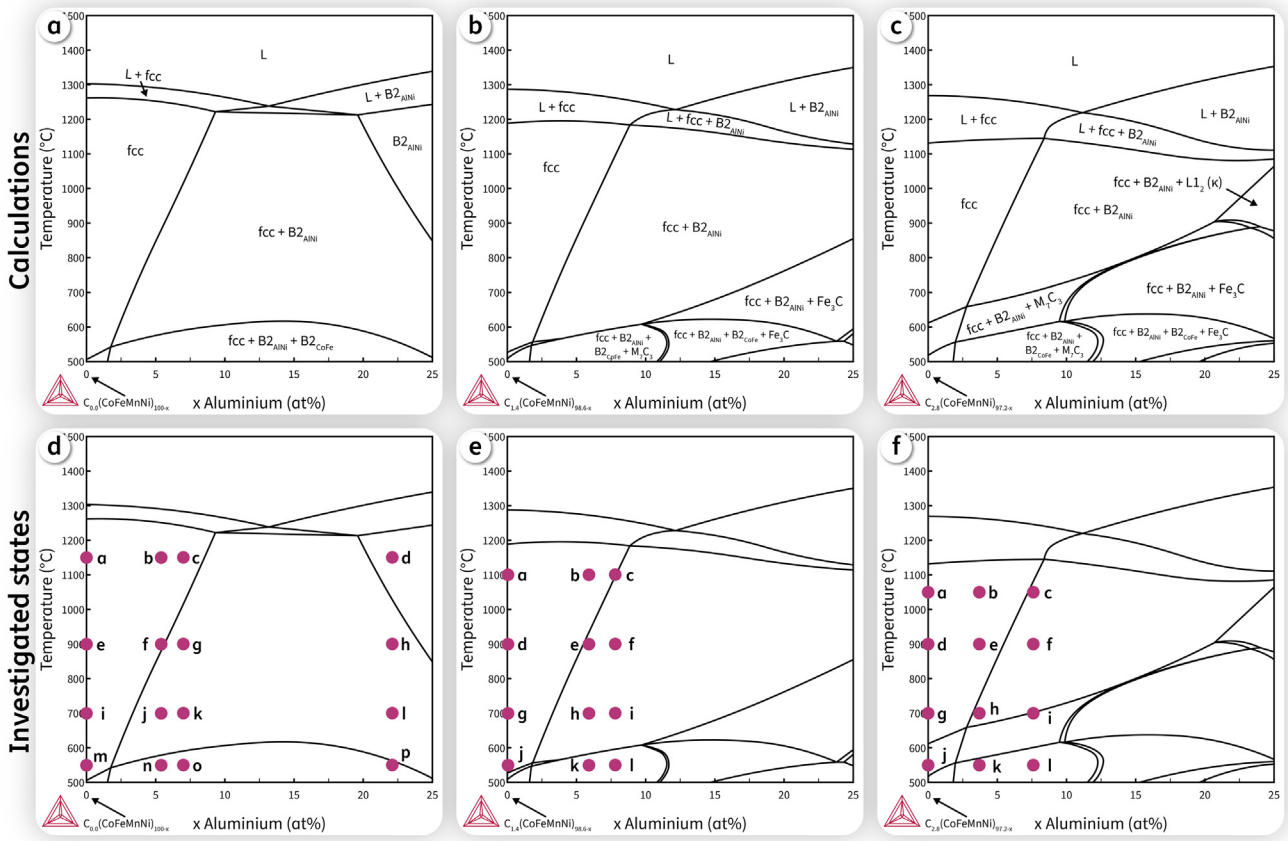

Fig. 1. Calculated vertical sections for the (a) $Al^xC^{0.0}$, (b) $Al^xC^{1.4}$ and (c) $Al^xC^{2.8}$ alloys using the custom CALPHAD database. The stable phases contained FCC, $B2_{NiAl}$ and $B2_{CoFe}$ ordered BCC phases and carbides (M_7C_3, Fe_3C and κ). (d–f) The investigated states are marked with points in the calculated phase diagrams.

Table 1
Chemical composition of the investigated samples from wet chemical analysis.

	(at.%)						(wt%)					
Sample	Al	C	Co	Fe	Mn	Ni	Al	C	Co	Fe	Mn	Ni
$Al^{0.0}C^{0.0}$	–	–	22.5	24.6	28.7	24.2	–	–	23.3	24.1	27.7	24.9
$Al^{0.0}C^{0.8}$	–	0.78	24.7	25.3	25.0	24.3	–	0.17	25.6	24.9	24.2	25.2
$Al^{0.0}C^{1.3}$	–	1.33	24.0	24.8	25.8	24.0	–	0.28	25.1	24.5	25.1	25.0
$Al^{5.4}C^{0.0}$	5.39	–	20.2	24.9	22.2	27.3	2.62	–	21.5	25.1	22.0	28.8
$Al^{5.9}C^{1.2}$	5.90	1.16	19.3	24.2	22.3	27.2	2.90	0.25	20.7	24.7	22.3	29.1
$Al^{3.7}C^{2.3}$	3.66	2.29	21.8	24.7	20.2	27.4	1.80	0.50	23.3	25.0	20.1	29.2
$Al^{7.0}C^{0.0}$	7.01	–	20.0	23.4	23.4	26.2	3.44	–	21.4	23.8	23.4	27.9
$Al^{7.8}C^{1.1}$	7.83	1.10	20.2	23.3	20.8	26.9	3.89	0.24	21.9	23.9	21.0	29.1
$Al^{7.6}C^{2.2}$	7.63	2.15	19.9	23.3	20.4	26.6	3.82	0.48	21.8	24.1	20.8	28.9
$Al^{22.1}C^{0.0}$	22.1	–	18.4	19.6	19.3	20.5	11.8	–	21.6	21.7	21.1	23.9

are stable at the performed annealing temperatures and may coarsen only at higher temperature [73] or longer annealing [74]. Therefore, O did not go into solution by the heat treatment and did not influence the phase stability or microstructure constitution. Furthermore, the comparatively low volume fraction and large particle size of the oxides has only a minor effect on the tensile test properties and may reduce strength slightly [75]. Therefore, the AM samples can be used to compare the materials properties for the investigated alloys.

The obtained chemical compositions (Table 1) were in the region of equiatomic composition, where the deviations were small with averages of ΔCo = -2.4 at.%, ΔFe = 0.6 at.%, ΔMn = -0.6 at.% and ΔNi = 2.4 at.% due to the usage of elemental powder blends [67,76,66]. The samples still allow the determination of the CoFeMnNi alloy's properties, as perfect equiatomicity was deemed an unnecessary requirement for the ideal properties in MPEAS [3]. Overall, the targeted compositions from the thermodynamic screening (Fig. 1) were hit with slight losses in Al and C. The exceptions were the C–containing $Al^{0.0}C^x$ alloy with lower-than-expected C contents and the $Al^{3.7}C^{2.3}$ alloy, where the Al content was lower than expected due to processing irregularities.

2.3. Microstructure characterization techniques

Samples for the microstructure analyses were prepared as following:

1. Mechanical grinding using 80, 180, 320, 600 and 1200 grit SiC paper.
2. Mechanical polishing using 6 and 1 μm diamond suspensions.
3. Electrolytical polishing at, depending on the chemical composition, 18 to 23 V for 15 s in Struers A2 electrolyte. The usage of electropolishing for sample preparation exaggerated the oxide volume fraction in the micrographs as oxides were not affected and stuck out of the surface.

Scanning electron microscopy (SEM) microstructure characterization techniques were made on a Zeiss Sigma field emission gun (FEG), where Oxford's electron backscatter diffraction (EBSD) and energy-dispersive X-ray spectroscopy (EDS) detectors were used. Using a voltage of 15 kV with a working distance between 7 and 9 mm, backscattered electron (BSE) micrographs and EDS measurements were recorded. For EBSD, 20 kV and 17 mm were used, respectively, with a step size of 60 nm. The EBSD data was analyzed using the MTEX toolbox [77,78] in MATLAB®.

Transmission electron microscopy (TEM) measurements were made on lamellae, which were taken from the samples by a FEI STRATA focused ion beam (FIB) 205 and measured on a FEI Tecnai F20 operated at 200 kV. Selected area electron diffraction (SAED) patterns were analyzed using the jems software [79].

X-ray diffraction (XRD) was performed on a SEIFERT Analytical X-ray diffractometer with 0.2289649 nm Cr-k_α radiation within a range of 60 ° to 160 ° for 2Θ. Diffraction patterns for synchrotron X-ray diffraction (SYXRD) were made on a Varex XRD 4343CT detector at DESY in Hamburg on the P02.1 beamline. Integration of complete rings in the patterns were performed using Fit2D [80,81] between 2.8° to 16.6° for 2Θ. Using Rietveld refinement in the open-source software Material Analysis Using Diffraction (MAUD) [82], the lattice parameters and phase fractions were determined for the XRD and SYXRD diffractograms.

2.4. Mechanical characterization techniques

Vickers microhardness was measured with a force of 0.9807N (HV0.1) on a polished surface of the microstructure samples. Three indentations were taken per sample.

Out of PBF-LB produced cylinders, round B4×20 tensile specimens were machined after DIN 50125 and tensile testing was performed on a Zwick/Roell Z4204. The quasi-static tests were performed at room temperature using a strain rate of 2.5×10^{-4} s^{-1} and the build-up direction was parallel to the straining direction.

3. Results

3.1. Thermodynamic calculations

Calculated vertical sections for the $Al^xC^{0.0,\ 1.4,\ 2.8}$ alloys between 500 to 1500 °C are shown in Fig. 1. In the $Al^{0.0}C^x$ alloy (Fig. 1a) at temperatures below the melting point, the FCC phase is prevalent in the alloy. With increased Al content a $B2_{NiAl}$ phase (ordered BCC) becomes stable, which at around ~20 at.% fully replaces the FCC phase. At temperatures below ~600 °C, the $B2_{CoFe}$ phase is stable in addition to $B2_{NiAl}$. In $Al^xC^{1.4}$ (Fig. 1b), the single-phase $B2_{NiAl}$ region is shifted to higher Al contents, i.e., the FCC phase is stabilized, while the M_7C_3 and Fe_3C carbides become stable at lower temperatures. Furthermore, the liquidus and solidus temperatures decrease in addition to an increased solidification interval. In $Al^xC^{2.8}$ (Fig. 1c), the FCC stability remains similar to the $Al^xC^{1.4}$ alloy with respect to the $B2_{NiAl}$ and $B2_{CoFe}$ regions, whereas the carbide regions shift to higher temperatures. Additionally, the $E2_1$ Perovskite-type κ-phase ($L1_2$ ordered FCC unit cell with a C atom in the center) becomes stable at high Al content at elevated temperatures. The points marked in Figs. 1d,1e,1f show all investigated states in this work.

3.2. Microstructure

The XRD measurement results at the points in the CALPHAD phase diagrams (Figs. 1d to f) can be found in Fig. 2. Regardless of the annealing state or C content, the $Al^{0.0}C^x$ alloys were fully FCC. In the homogenized states (Figs. 2a to c), fully FCC microstructures were detected in the alloys $Al^{\sim 5.0}C^x$, where the C content had no effect on the occurring phases. At higher Al contents in the $Al^{\sim 7.5}C^x$ and $Al^{22.1}C^{0.0}$ alloys, the microstructure contained a $B2_{NiAl}$ phase at the cost of FCC peak intensity. The $B2_{NiAl}$ phase also appeared after annealing of the $Al^{\sim 5.0}C^x$ alloys at 900 and 700 °C and at higher Al contents (Figs. 2d to i). In the alloys $Al^{\geq 5.4}C^x$ annealed at 550 °C (Figs. 2j,k,l), $B2_{NiAl}$ peaks were detected in addition to $B2_{CoFe}$ peaks, where considerable peak broadening took place. The peak intensities of $B2_{NiAl}$ and $B2_{CoFe}$ increased with increasing Al content. In summary, increased amount of $B2_{NiAl}$ were detected with higher Al content and annealing at 550 °C resulted in the formation of $B2_{CoFe}$, while the C content had a negligible effect. Samples with high Al content (mainly $Al^{22.1}C^{0.0}$) additionally showed weak superlattice reflections of the $B2_{NiAl}$ phase.

The lattice parameters and phase fractions calculated from the XRD measurements (Fig. 2) are summarized in Fig. 3. The lattice parameter of the FCC phase (Fig. 3) increased on average by 0.003 Åat.%$^{-1}$ Al and 0.002 Åat.%$^{-1}$ C. The FCC lattice parameters varied slightly with the annealing temperature without any clear trend. Two lattice parameters for $B2_{NiAl}$ and $B2_{CoFe}$ (Fig. 3b) were identified and showed no clear dependence on the annealing temperature or chemical composition. The average lattice parameters for $B2_{NiAl}$ and $B2_{CoFe}$ were 2.895 Å and 2.869 Å, respectively. The phase fractions of the B2 phases (Fig. 3c) increased with higher Al content with a strong increase in $Al^{\sim 7.5}C^x$. The highest fraction of the $B2_{NiAl}$ phase was observed after annealing at 700 °C. In $Al^{7.6}C^{2.2}$ annealed at 550 °C, high fractions of the $B2_{NiAl}$- and $B2_{CoFe}$-phase were obtained.

Micrographs of the $Al^xC^{0.0}$ alloy are shown in Fig. 4. Regardless of the annealing temperature, fully FCC microstructures were found in the $Al^{0.0}C^{0.0}$ alloy. A fully FCC microstructure was also obtained in the $Al^{5.4}C^{0.0}$ alloy annealed at 1150 °C (Fig. 4b). At 900 °C (Fig. 4f), two additional types of secondary phases were detected with an island morphology at grain boundaries and plate morphology in the FCC matrix, which developed finer at 700 °C (Fig. 4j). At 550 °C (Fig. 4n), fine plate-type precipitates were found at the grain boundaries. In the $Al^{7.0}C^{0.0}$ alloy annealed at 1150 °C (Fig. 4c), small amounts of the island-type phase were detected at the grain boundaries of a fully FCC matrix. The microstructures at 900 and 700 °C (Figs. 4g,k) were similar to that of $Al^{5.4}C^{0.0}$, albeit with higher volume fractions of the island- and plate-type phases. At 550 °C, high volume fractions of fine precipitates were found in the matrix with small amounts of the island phase at the grain boundaries. In the alloy $Al^{22.1}C^{0.0}$, a dual-phase microstructure was obtained at 1150 °C (Fig. 4d). At 900 and 700 °C (Figs. 4h,l), the formation of the plate-type phase was observed in the indented grains. The plate thickness decreased on average from 370 to 180 nm after annealing at 900 and 700 °C, respectively. Fine precipitates were formed at 550 °C (Fig. 4p) in the deep etched grains of the microstructure. Overall, a higher Al content in $Al^xC^{0.0}$ resulted in higher amounts of the island- and plate-type

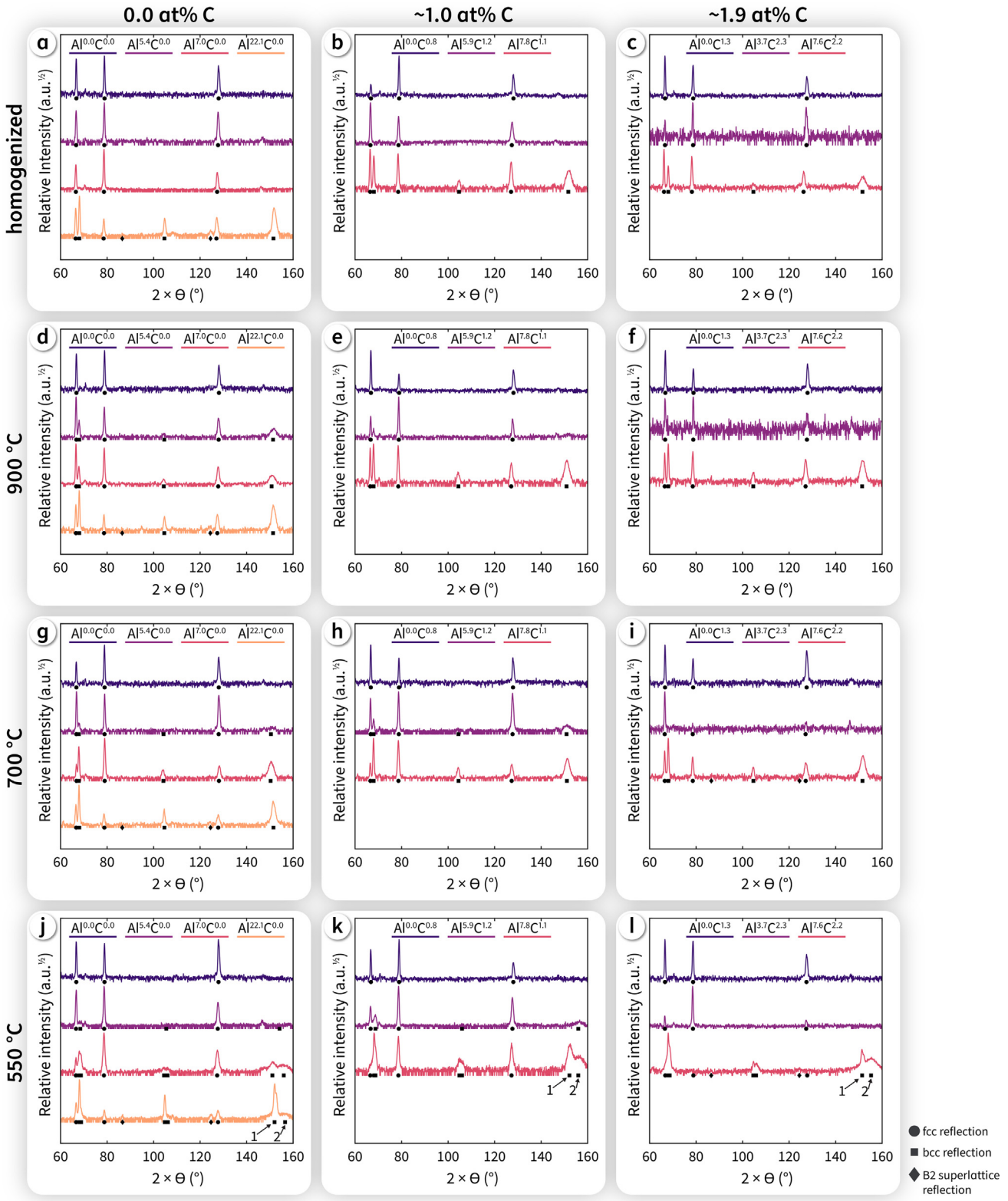

Fig. 2. XRD diffractograms of the investigated alloys in the (a–c) homogenized, (d–f) 900°C, (g–i) 700°C and (j–l) 550°C annealed states with peak assignments for FCC, BCC and B2 superlattice reflections. At (j–l) 550°C annealing and high Al contents, two separate BCC_1 and BCC_2 phases were identified, which were determined to be $B2_{NiAl}$ (see Fig. 8) and $B2_{CoFe}$ (see Fig. 9), respectively. The calculated lattice parameters and volume fractions for the different phases can be found in Fig. 3.

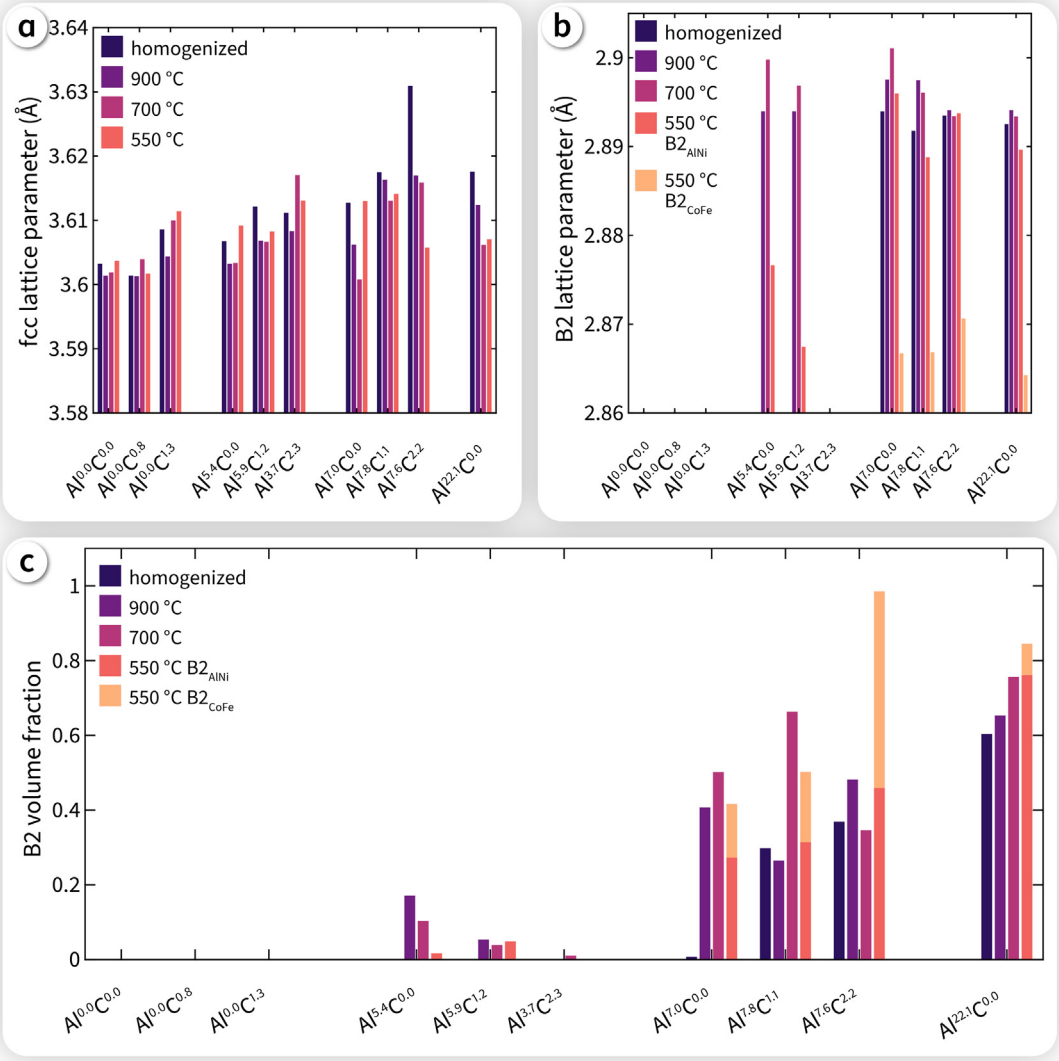

Fig. 3. Influence of the chemical composition and heat treatment on the calculated (a–b) lattice parameters and (c) bcc volume fractions from the XRD measurements shown in Fig. 2 (the exact values can be found in the supplementary material). The FCC lattice parameter increased with Al and C, while only the volume fraction increased for the B2 phases.

microstructural features at 900 and 700 °C. The plate-type microstructure formed the FCC matrix, while the island-type phase formed at grain boundaries. Al-containing samples showed the formation of fine precipitates at 550 °C inside the FCC matrix.

Micrographs for the $Al^{x}C^{\sim 1.0}$ alloys can be found in Fig. 5. Similar to the $Al^{0.0}C^{0.0}$ alloy and regardless of annealing temperature, the $Al^{0.0}C^{0.8}$ alloy showed a fully FCC microstructure. A fully FCC microstructure was also obtained in the $Al^{5.9}C^{1.2}$ alloy annealed at 1100 °C (Fig. 5b). At 900 and 700 °C (Figs. 5e,h), the formation of the island- and plate-type phases were detected. The plate thickness decreased on average from 290 to 230 nm after annealing at 900 and 700 °C, respectively. At 550 °C (Fig. 5k), the formation of basketweave-type precipitates occurred at grain boundaries. The microstructure developed similarly in the $Al^{7.8}C^{1.1}$ alloy with higher volume fractions of the island- and plate-type phases. The basketweave-phase precipitates at 550 °C (Fig. 5l) were found in the FCC matrix of the microstructure. Overall, the microstructure in $Al^{x}C^{\sim 1.0}$ developed similarly to the $Al^{x}C^{0.0}$ alloys, where higher Al contents resulted in the formation of island- and plate-type phases as well as fine precipitates in Al-containing samples at 550 °C.

Micrographs of the $Al^{x}C^{\sim 1.9}$ alloys are presented in Fig. 6. The $Al^{0.0}C^{1.3}$ alloy showed a fully FCC microstructure. Due to the low Al content, the $Al^{3.7}C^{2.3}$ alloy was fully FCC at the investigated annealing temperatures with small amounts of island-type phases at 700 °C (Fig. 6h). At 550 °C (Fig. 6k), a fully FCC microstructure was obtained. In the $Al^{7.6}C^{2.2}$ alloy, the island-type phase was seen at 1050 °C, while at 900 and 700°C the formation of plate-like phases was observed. The plate thickness decreased on average from 810 to 210 nm after annealing at 900 and 700 °C, respectively. At 550 °C (Fig. 6l), basketweave-type precipitates formed between the island-type phase. Overall, except for the low Al-containing $Al^{3.7}C^{2.3}$ alloy, the formation of the island-, plate- and basketweave-type phases developed similar to alloys without C (Figs. 4,5).

3.3. Detailed microstructure analysis

To investigate the microstructure in Al- and C-added CoFeMnNi, more detailed analyses were performed on a subset of the samples. Even though 40 different chemistry-annealing combinations were investigated, clear trends in microstructure evolution and the con-

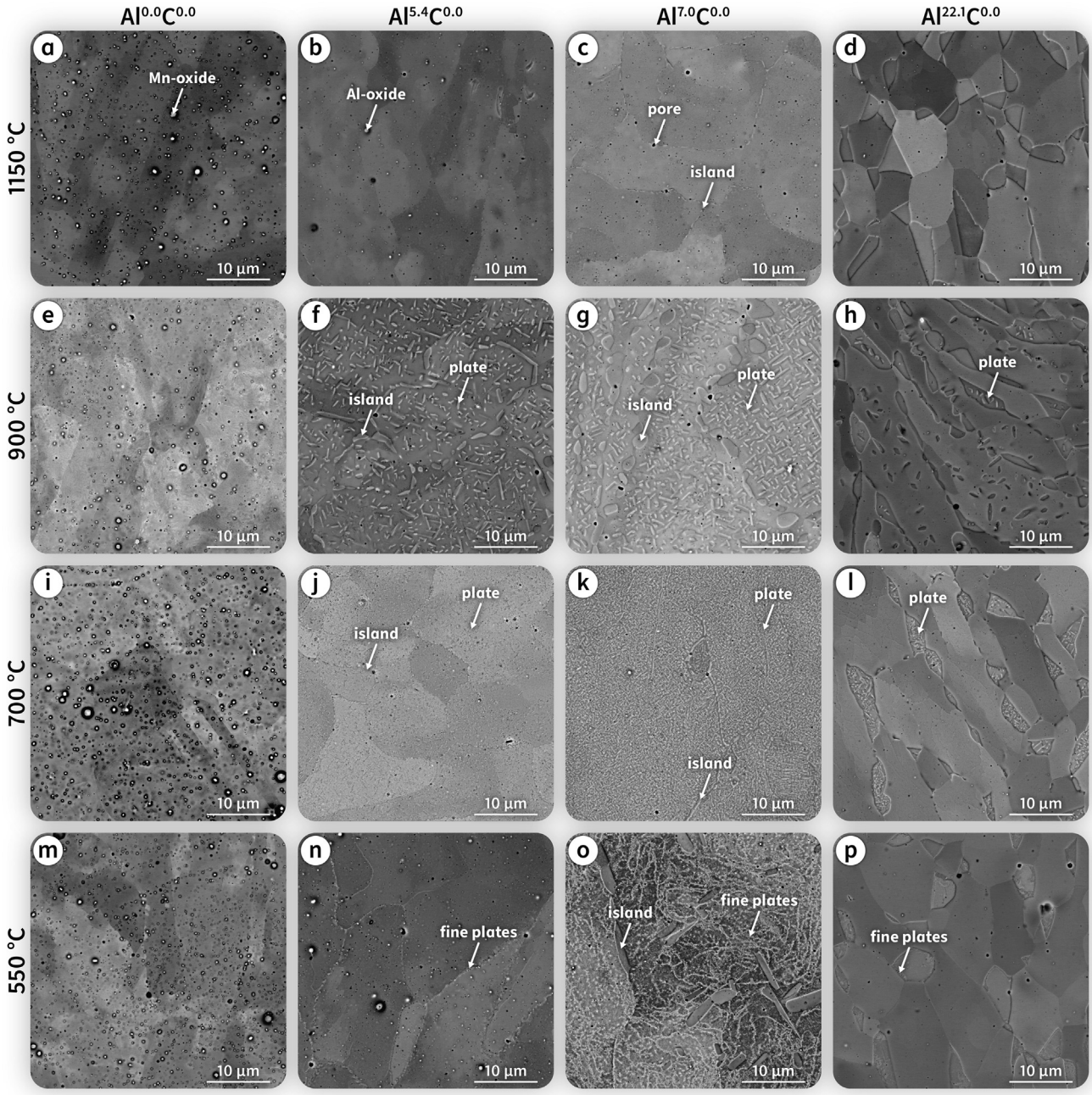

Fig. 4. BSE micrographs of the alloys indicated by the points shown in the Fig. 1d phase diagram. Pores, Mn and Al oxides were introduced into the samples by the PBF-LB sample manufacturing process and the typical AM microstructure features were removed by the homogenization annealing. FCC-based microstructures were obtained with island- (1150°C) and plate-type (⩽900°C) precipitates at higher Al contents.

tained phases were observed. The $Al^{22.1}C^{0.0}$ alloy showed a dual-phase microstructure, and three types of precipitate morphologies were observed: island-, plate- and basketweave-type precipitates. Representative samples showing these microstructure morphologies were analyzed in more detail.

A dual-phase microstructure developed in the $Al^{22.1}C^{0.0}$ due to the high Al content (Fig. 4d), which was analyzed by EBSD and EDS (Fig. 7). The morphology (Figs. 7a and b) consisted of large $B2_{NiAl}$ grains with smaller FCC islands. The $B2_{NiAl}$ phase was rich in Al and Ni, while Co, Fe and Mn had higher concentrations in the FCC phase.

Analysis of the island- and plate-type phases was performed in the $Al^{7.8}C^{1.1}$ alloy annealed at 700 °C and is shown in Fig. 8. EBSD (Figs. 8a and b) revealed that both precipitate morphologies had a BCC crystal structures. The simultaneous EDS analysis (Figs. 8c to g) showed that both precipitates were enriched in Al and Ni and depleted in Co and Fe. TEM analysis of the island-type phase (Figs. 8h to k) was performed to gain additional information about the crystal structure in both morphologies. A B2 crystal structure was observed in the SAED pattern (Fig. 8k) with superlattice reflections for the [011] zone axis. Additionally, reflections for a B2 phase with a [113] zone axis (Fig. 8j) were detected in the SAED pattern from a phase contained within the TEM lamella. The Al and Ni rich island- and plate-type precipitates were $B2_{NiAl}$ phases.

A detailed analysis of the fine plate-type precipitates was performed on the $Al^{7.0}C^{0.0}$ alloy annealed at 550 °C is shown in Fig. 9. Higher magnification BSE micrographs (Figs. 9a,b) showed a plate-like morphology. The SYXRD analysis (Figs. 9c,d) revealed one

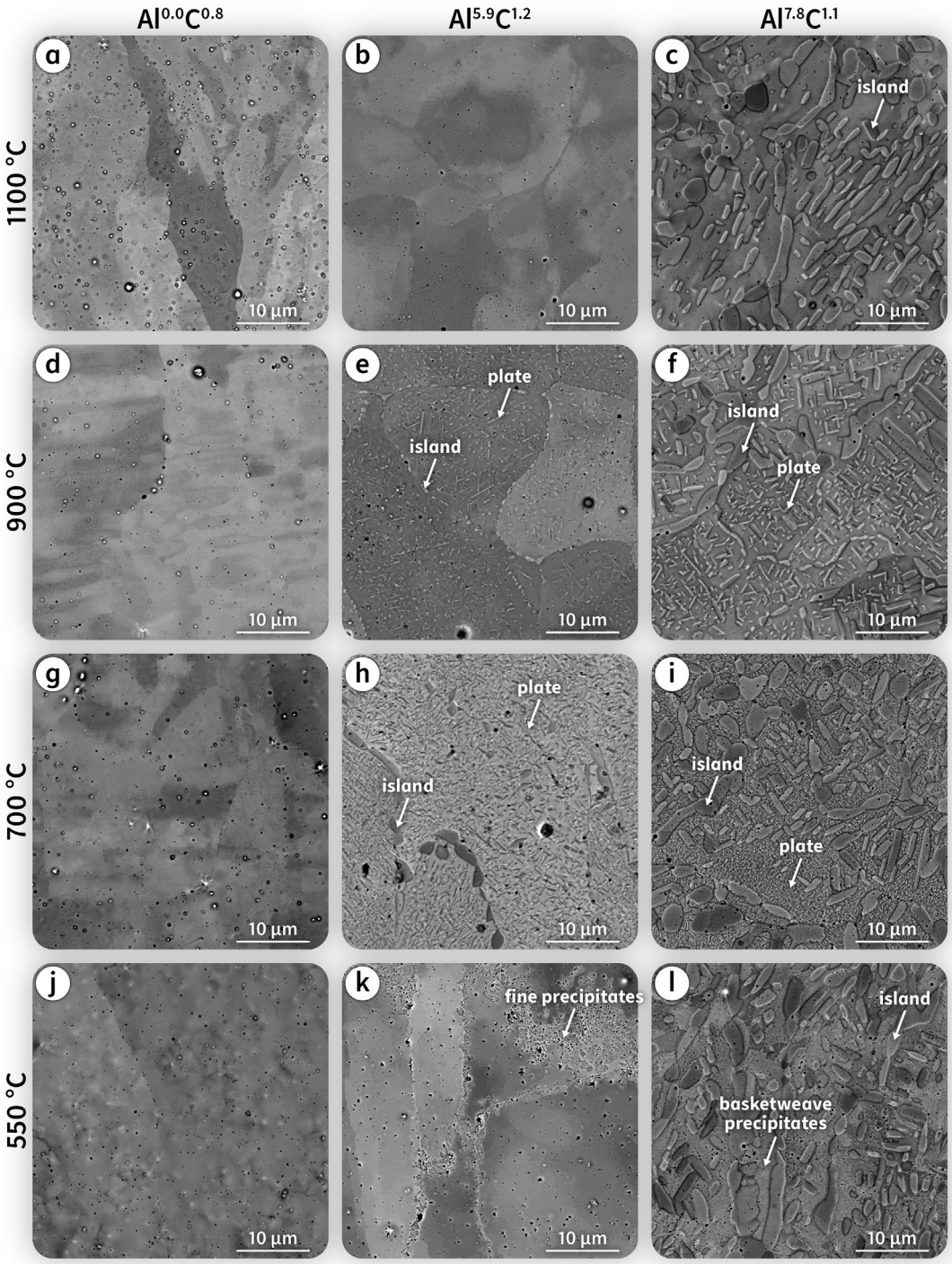

Fig. 5. BSE micrographs of the alloys indicated by the points shown in the Fig. 1e phase diagram. FCC-based microstructures were obtained with island- (1100°C), plate- (900 to 700°C) and basketweave-type (550°C) precipitates at higher Al contents.

FCC (3.626 Å lattice parameter) and two BCC phases in the microstructure. The superlattice reflections at (100) and (111) for the B2 phase were clearly visible but could not be attributed unambiguously to either one of the BCC phases due to peak overlap. The Rietveld refinement was performed with ~30 at.% dissolved other constituting elements on the lattice sites in the B2 phase, i.e., lower amount of B2 ordering, to sufficiently fit the superlattice reflections. Phase fractions of 15.6 and 10.0 % and lattice parameters of 2.913 and 2.876 Å were obtained for the $B2_{NiAl}$ and $B2_{CoFe}$ phase, respectively. Increased peak widening in the $B2_{NiAl}$ phase compared to the $B2_{CoFe}$ peaks indicated a finer precipitate size for $B2_{NiAl}$. In the TEM analysis, fine plates were observed in the FCC matrix (Figs. 9e and g) with a thickness of 20 nm. Compared to the FCC matrix, these plates were enriched in either Co + Fe (Fig. 9f) or Al + Ni (Fig. 9h), corresponding to the two different B2 phases identified by the SYXRD analysis. The diffraction analysis (Figs. 9i to l) revealed a FCC matrix with a [011] zone axis next to B2 with a [011] zone axis containing faint superlattice reflections. The resulting orientation relationship between the phases was $\{111\}_{fcc}\|\{110\}_{B2}$ and $\langle 011\rangle_{fcc}\|\langle 011\rangle_{B2}$. In summary, the ordered

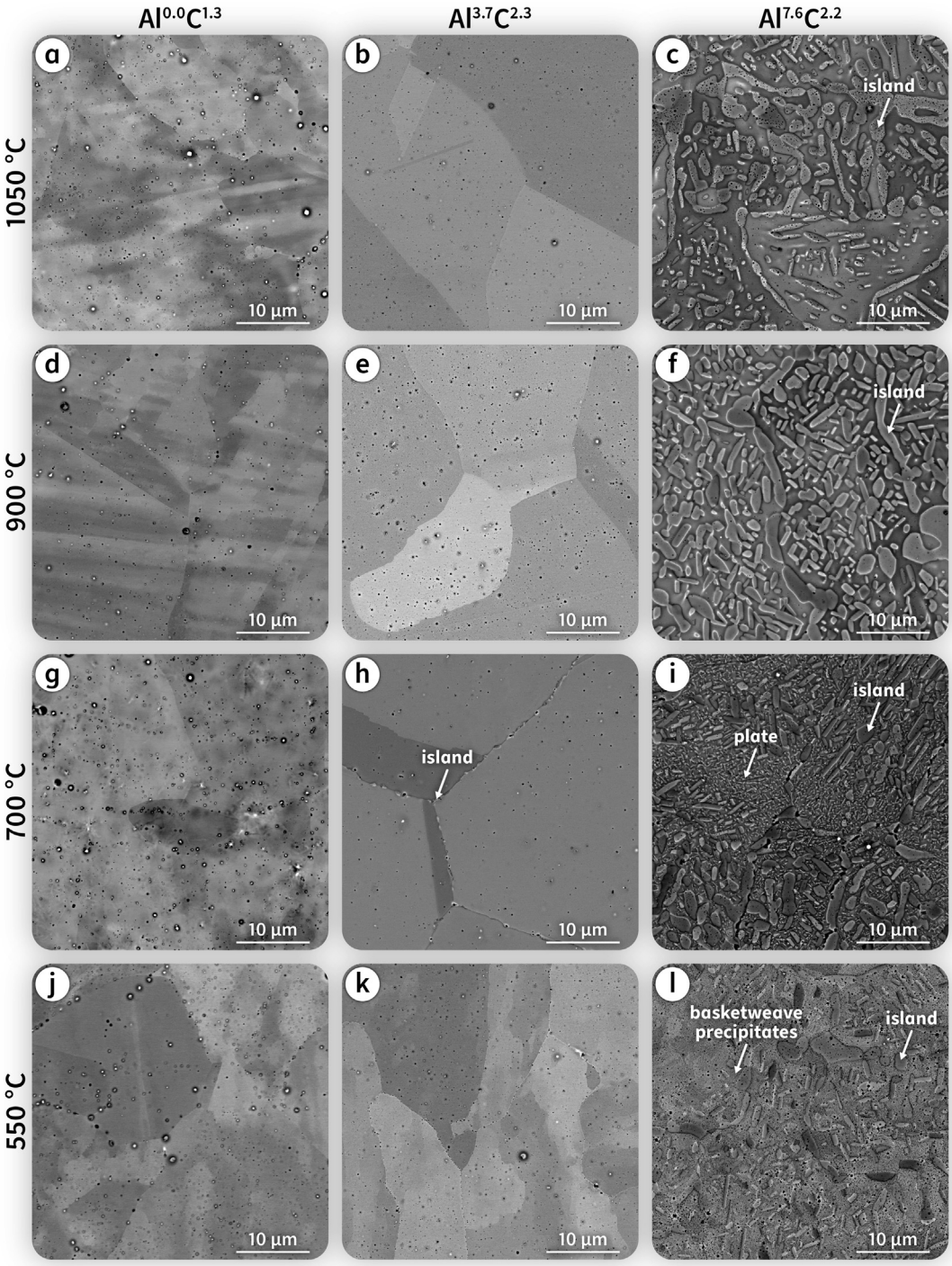

Fig. 6. BSE micrographs of the alloys indicated by the points shown in the Fig. 1f phase diagram. Due to a low Al content in the $Al^{3.7}C^{2.3}$ alloy, few precipitates were formed after annealing. FCC-based microstructures were obtained with island- (1050°C), plate- (900 to 700°C) and basketweave-type (550°C) precipitates at higher Al contents.

BCC phases $B2_{NiAl}$ and $B2_{CoFe}$ were found to precipitate in plates in the FCC matrix.

The formation of the basketweave-type precipitates in Al- and C–containing alloys annealed at 550 °C was analyzed for the $Al^{7.6}C^{2.2}$ alloy in Fig. 10. In the higher magnification BSE micrographs (Figs. 10a and b), the formation of fine precipitates was observed with lamella-type precipitates in between a decomposed matrix. The SYXRD analysis (Figs. 10c,d) revealed a FCC matrix phase (3.639 Å) with the highest intensity containing peaks for the $B2_{NiAl}$- (2.901 Å), $B2_{CoFe}$- (2.874 Å), $L1_2$- (3.658 Å) and M_7C_3-phases. The superlattice reflections for $B2_{NiAl}$ and $L1_2$ were clearly visible. Due to a very fine precipitation size, the peaks for the $L1_2$ phase were broadened considerably. The high-resolution STEM and EDS analysis (Figs. 10e,h) revealed 17 nm diameter cubic precipitates in the decomposed FCC matrix with 31 nm thick lamellar phase in between. The lamellar phase was enriched in Mn + C (Fig. 10f) and the cubic precipitates in either Co + Fe or Al + Ni (Fig. 10h). As evidenced by the TEM diffraction analysis (Figs. 10i to k), the lamellar phase contained the M_7C_3-type carbide phase

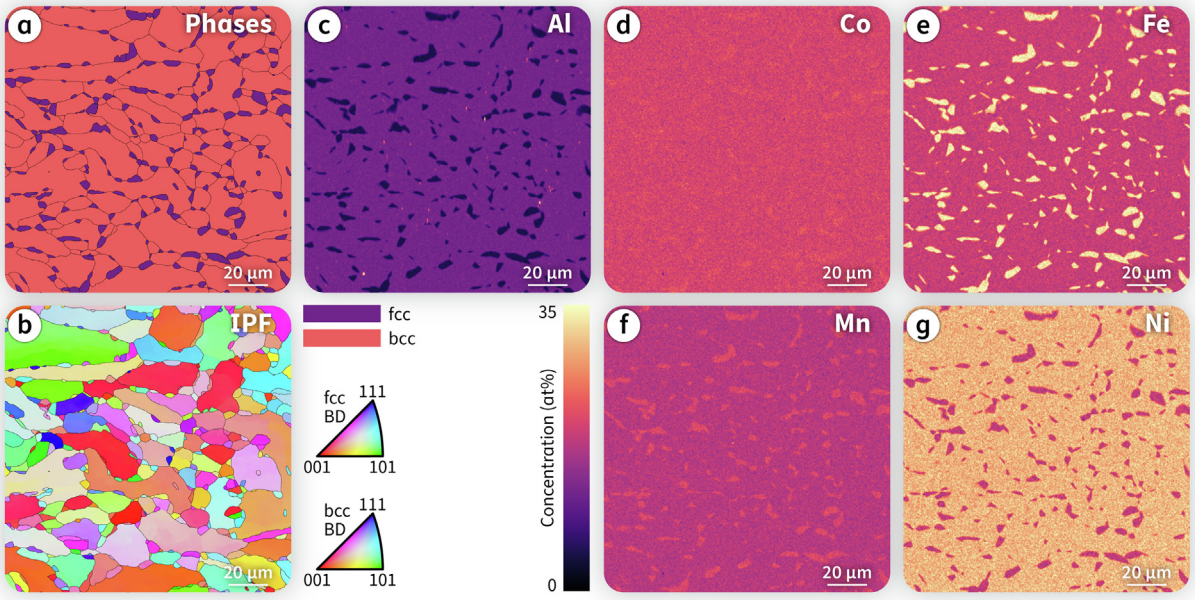

Fig. 7. (a–b) EBSD and (c–g) simultaneous EDS analysis of the dual-phase microstructure in the $Al^{22.1}C^{0.0}$ alloy in the homogenized state (Fig. 4d). The detected BCC phase was enriched in Al and Ni and found to be $B2_{NiAl}$ (see Fig. 8). (c) The small Al peaks were caused by Al oxide formation.

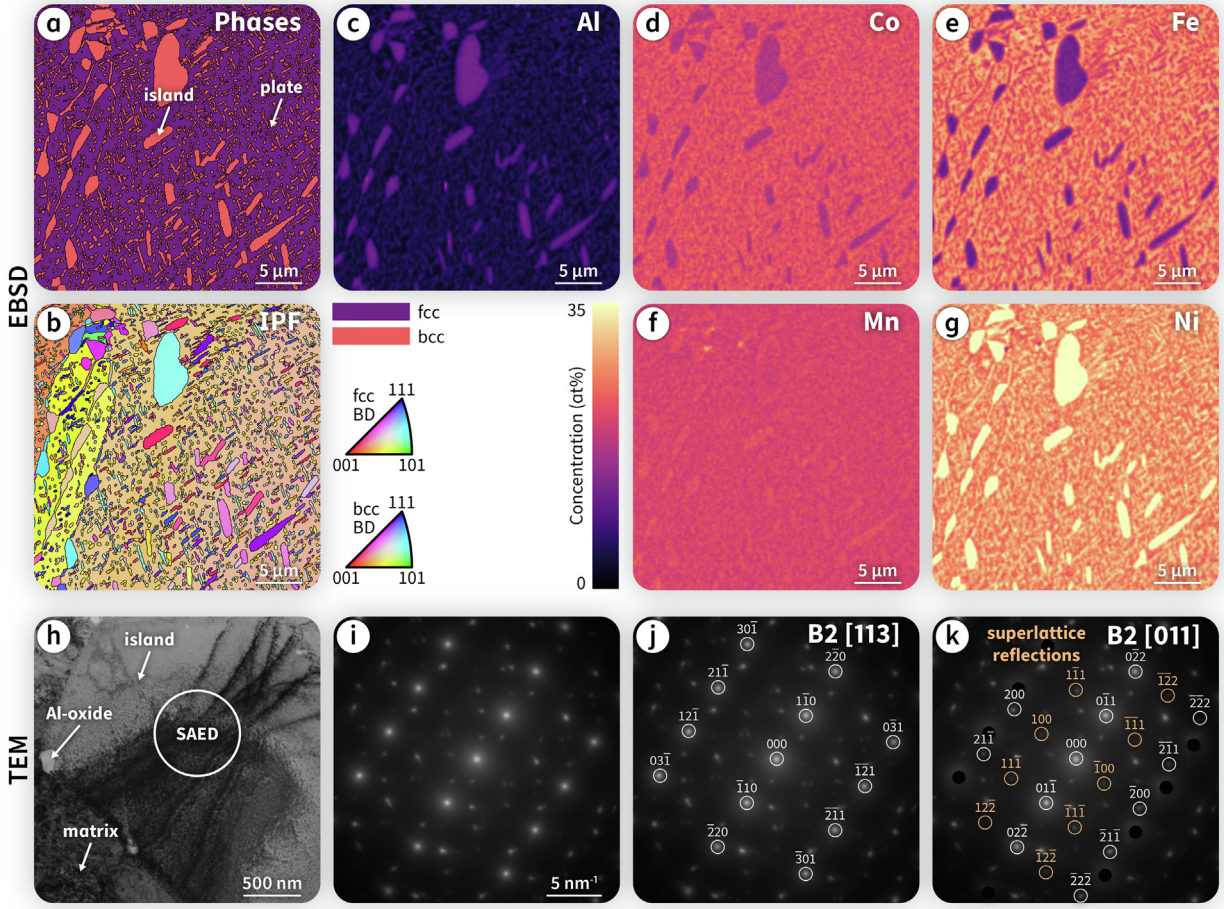

Fig. 8. (a–b) EBSD and (c–g) simultaneous EDS of the island- and plate-type precipitates in the $Al^{7.8}C^{1.1}$ alloy annealed at 700°C (Fig. 5i). The BCC phases were enriched in Al and Ni and found to be (f) $B2_{NiAl}$. (c) The small Al peaks were caused by Al oxide formation. The (h) high-angle annular dark field (HAADF) micrograph and (i–k) SAED pattern analysis revealed the islands as a $B2_{NiAl}$ phase.

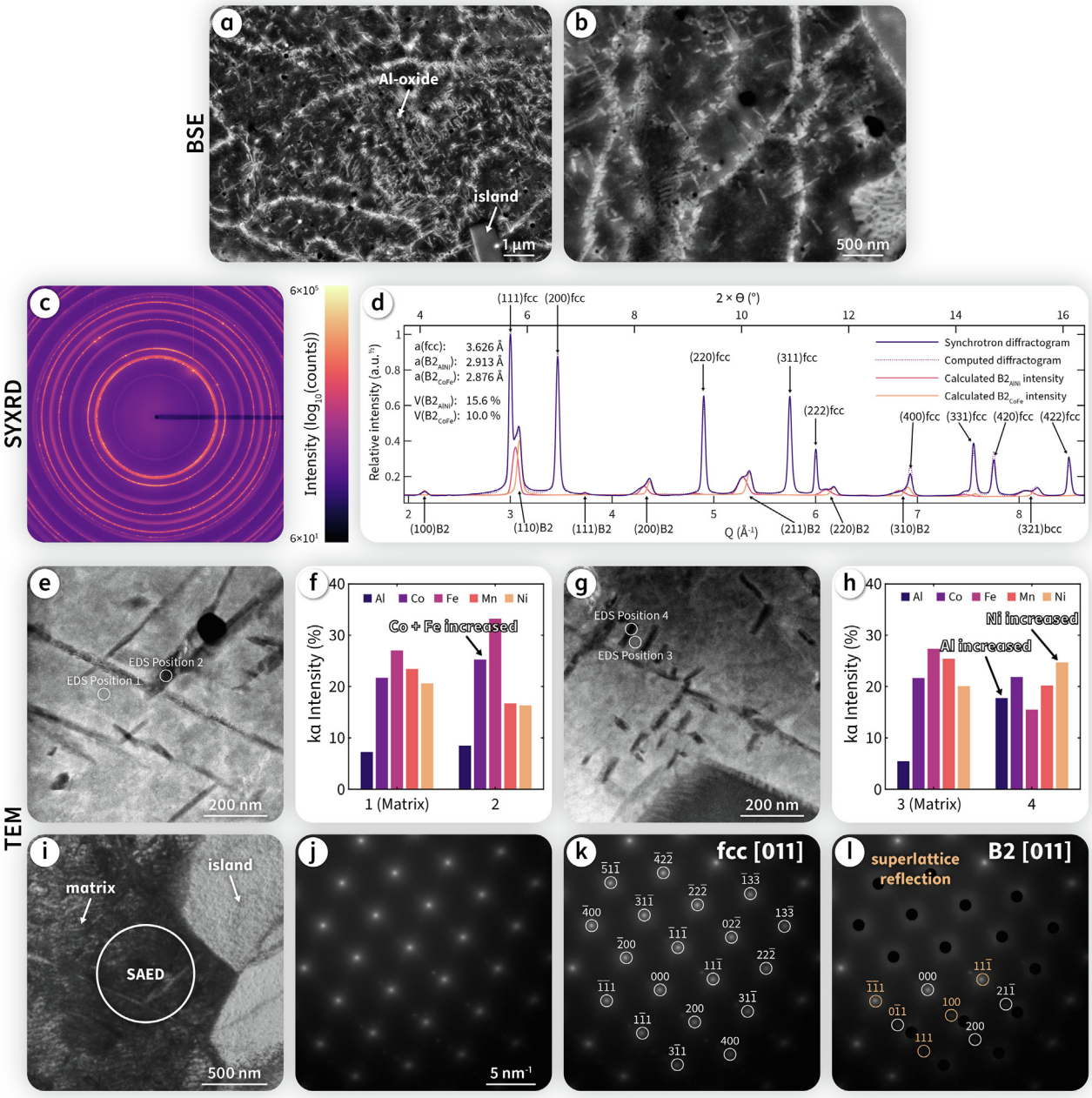

Fig. 9. Analysis of the fine plate-type precipitates in the $Al^{7.0}C^{0.0}$ alloy annealed at 550°C (Fig. 4o), which were detected by (a–b) BSE micrographs. (c) The synchrotron ring pattern and (d) the corresponding integrated diffractogram revealed two B2 phases in the FCC microstructure (the lattice constants *a* and volume fractions *V* from the Rietveld refinement are also given). According to (e, g) the HAADF micrographs and (f, h) scanning transmission electron microscopy (STEM)-EDS analysis, the fine plates were enriched in either Al + Ni or Co + Fe. (i) The HAADF micrograph with (j–l) SAED analysis also revealed the plates as B2 phases.

with [011] zone axis. In this zone axis, the M_7C_3 phase showed multiple superlattice reflections ordered along lines (Fig. 10l). The cubic precipitates were found to be B2 ([001] zone axis) and $L1_2$ ([112] zone axis) crystal structures with their superlattice reflections (Figs. 10m to p). Additionally, reflections of a B2 phase with a [113] zone axis (Fig. 10o) were detected in the SAED pattern from a phase contained within the TEM lamella. As $L1_2$ was found next to FCC, the allowed FCC lattice reflections can be assigned to both phases. The resulting orientation relationship between the phases was $\{011\}_{fcc}\|\{001\}_{B2}$ and $\langle 112\rangle_{fcc}\|\langle 001\rangle_{B2}$. The M_7C_3 formed with a lamellar morphology in the FCC matrix, while fine cuboidal $L1_2$ and $B2_{CoFe}$ precipitates enriched in Co + Fe or Al + Ni were found in the matrix.

3.4. Mechanical properties

The hardness of the investigated alloys is shown in Fig. 11. In the low Al-containing $Al^{0.0}C^{x}$ and $Al^{\sim 5.0}C^{x}$ alloys the hardness reached ~200 HV0.1, where it increased slightly with higher C content and small effects of the annealing temperature were seen. In the $Al^{\sim 7.5}C^{x}$ alloys, lower annealing temperatures increased the hardness strongly. Additionally, higher C content also strongly increased hardness up to 791 HV0.1 in $Al^{7.6}C^{2.2}$ annealed at 550 °C. In the $Al^{22.1}C^{0.0}$ samples, lower annealing temperatures resulted in higher hardness.

The tensile test data resulting from different outlined microstructures are plotted as Ashby plots in Fig. 12. Four types

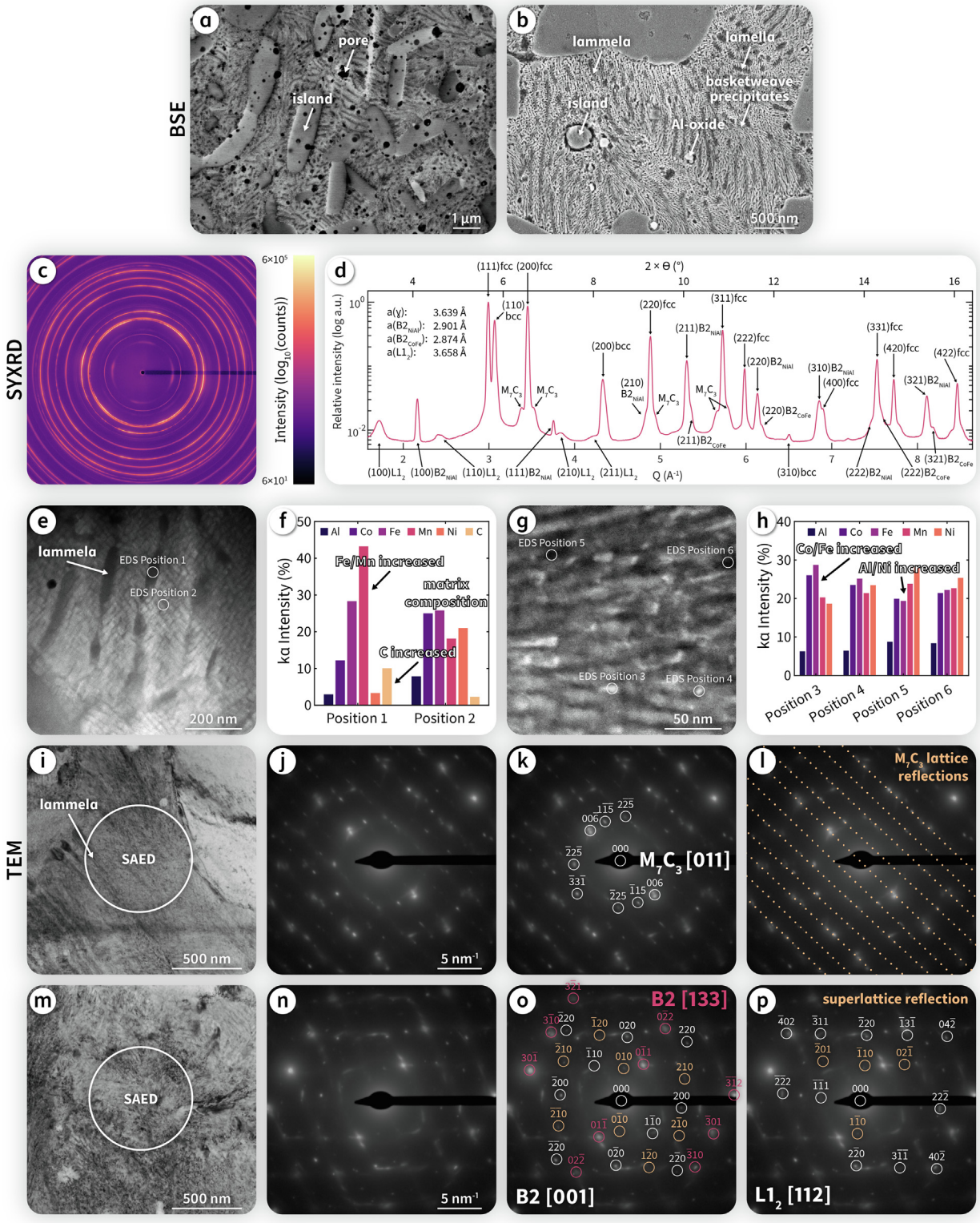

Fig. 10. Analysis of the basketweave-type precipitates in the $Al^{7.6}C^{2.2}$ alloy annealed at 550°C (Fig. 6l), which were detected by (a–b) BSE micrographs. (c) The synchrotron ring pattern and (d) the corresponding integrated diffractogram revealed $B2_{NiAl}$-, $B2_{CoFe}$- and $L1_2$-phases (the lattice constants a and volume fractions V are also given). Peaks belonging to a M_7C_3-type carbide were also detected. In the (e) HAADF micrograph and (f) STEM-EDS analysis, the lamellar phase had higher C, Fe and Mn k_α peak intensities compared to the surrounding microstructure. The cubic precipitates were (g–h) either rich in Ni + Al or Co + Fe. (i–l) In the SAED analysis containing the lamellar phase, the M_7C_3-type carbide was detected. (m–p) The SAED analysis containing the cubic precipitates revealed B2 and $L1_2$ phases.

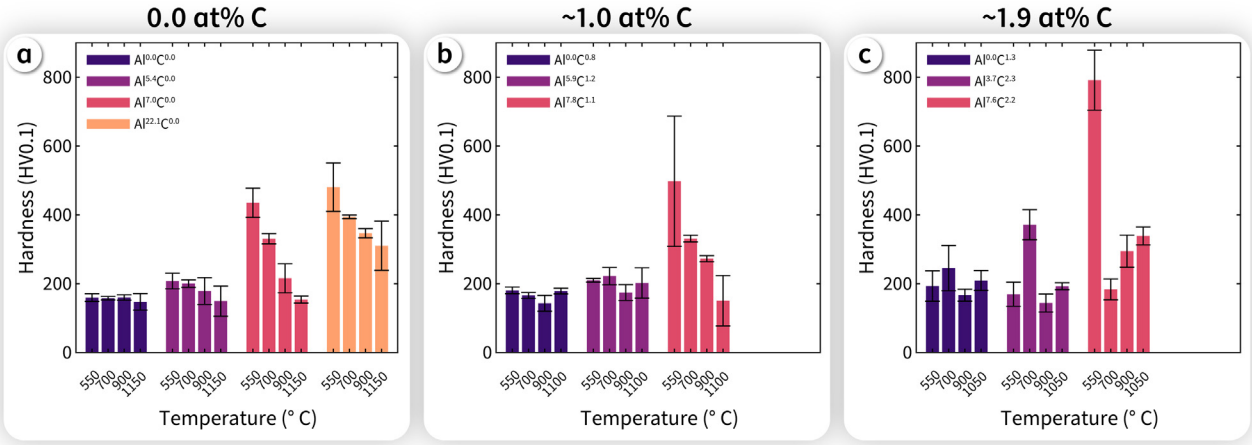

Fig. 11. Mean hardness with standard deviation as a function of Al content and annealing temperature of the investigated states with increasing C content at (a) 0.0at.%, (b) ~1.0at.% and (c) ~1.9at.%.

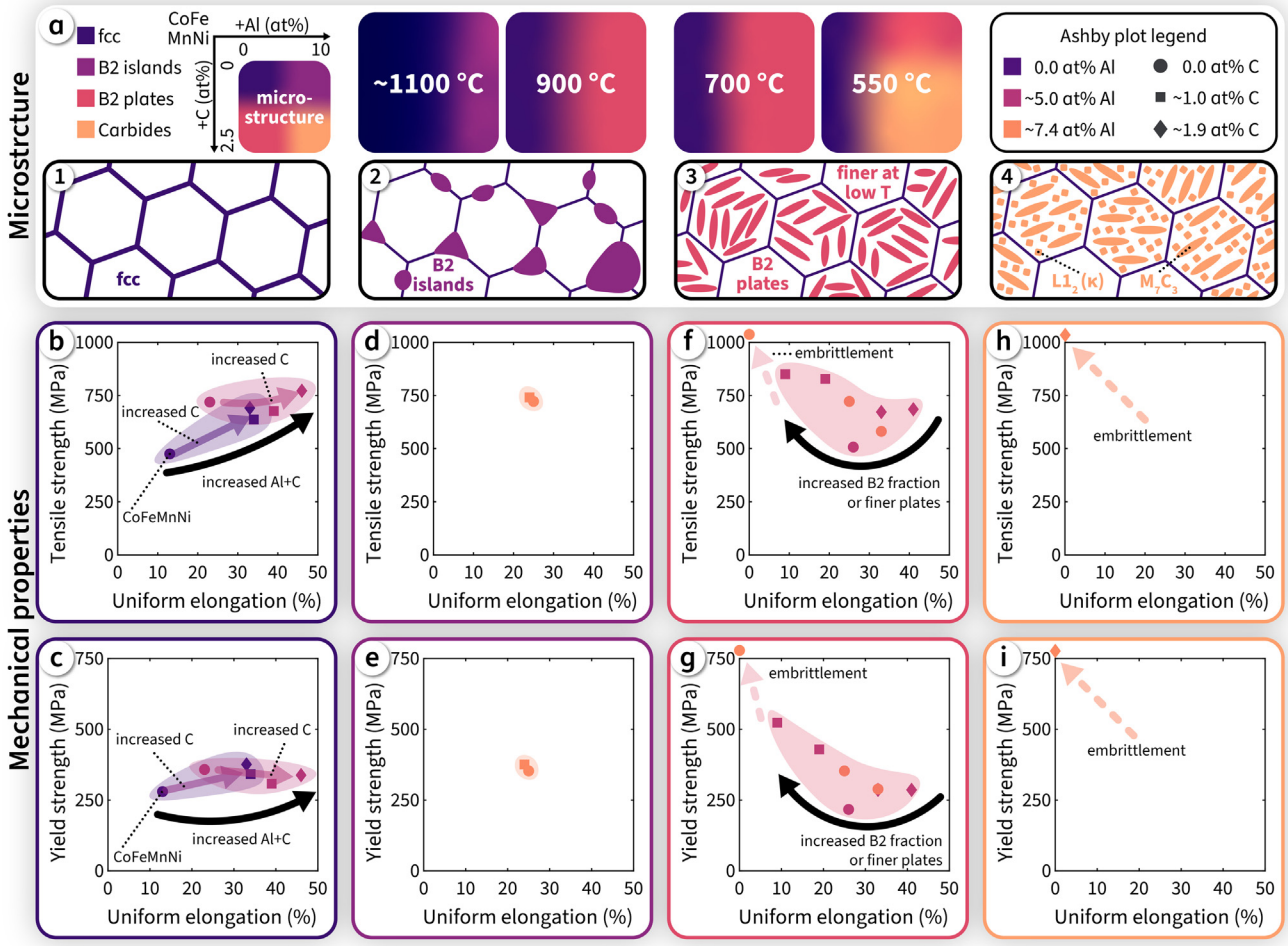

Fig. 12. (a) Schematic microstructures found in Al- and C-added CoFeMnNi (see micrographs in Figs. 4–6, *not to scale*). Four types of microstructural features occurred and are shown as a function of temperature, where the colors represent the microstructure type. (b–i) Ashby plots were created based on tensile tests performed on samples in the four microstructure states (based on ultimate tensile strength R_m, yield strength $R_{p0.2}$ and uniform elongation A_g; see supplementary material for tensile test data). The plots show the influence on the mechanical properties in (a1: b–c) FCC-based microstructures with (a2: d–e) B2 island-type, (a3: f–g) B2 plate-type and (a4: h–i) carbide precipitates.

of microstructures were observed in Al- and C-added CoFeMnNi (Fig. 12a).

1. Single-phase FCC microstructures were obtained below ~7 at.% Al with up to 2.5 at.% C between 1100 to 550 °C. The CoFeMnNi base alloy had 475 MPa R_m, 280 MPa $R_{p0.2}$ and 13 % A_g (Figs. 12b, c). An increase in C resulted in a strong increase in R_m and A_g, while the $R_{p0.2}$ increased slightly. The addition of Al had a similar effect. The combined addition of Al and C resulted in a further increase in R_m and A_g.
2. B2 island-type phases in the FCC microstructure were found above ~7 at.% Al with up to 2.5 at.% C between 1100 to 550 °C. This type of microstructure resulted in ~750 MPa R_m, ~380 MPa $R_{p0.2}$ and ~25% A_g (Figs. 12d,e). Compared to Al-added single-phase FCC CoFeMnNi, the elongation was decreased with similar strength.
3. B2 plate-type precipitates in the FCC microstructure were found above ~5 at.% between annealing temperatures of 900 to 550 °C. From 900 to 700 °C this region became stable at lower Al contents at 0 to 2.5 at.% C, while at 550 °C it was only obtained without C. Compared with the single-phase FCC alloys (Figs. 12b,c), the precipitation of B2 plates resulted in higher R_m and $R_{p0.2}$ at the cost of lower A_g (Figs. 12f,g). Increased fractions or finer plates (at lower annealing temperatures) resulted in strength increases up to brittle behavior at extremely fine plates.
4. κ- and M_7C_3-type carbide precipitates were seen at 550 °C annealing above ~5 at.% Al and ~1 at.% C. The tensile tests showed embrittlement in the samples with failure in the elastic region (Figs. 12h,i).

4. Discussion

40 states with different chemical compositions and varying annealing conditions were investigated in detail with respect to their microstructure and mechanical properties in Al- and C-added equiatomic CoFeMnNi MPEAs. To elucidate the individual and combined effects of the alloying elements Al and C, the discussion was structured as follows. First, the properties of the FCC-based CoFeMnNi parent alloy compared to other FCC-based MPEAs is highlighted in Section 4.1. The influences of C and Al on the microstructures and properties are then discussed separately Sections 4.2, as well as combined in Section 4.4.

4.1. Microstructure and properties of the CoFeMnNi alloy

The microstructure of the CoFeMnNi alloy was single-phase FCC at annealing temperatures ⩾550 °C with a lattice parameter of 3.603 Å (Figs. 2–4). Studies investigating the microstructure of CoFeMnNi [83,84] also obtained fully FCC microstructures, albeit the investigations were only performed on as-cast and homogenized material. The results coincided with the phase compositions found in variations of 3d transition element MPEAs [3], where single-phase FCC alloys were typically observed. Multi-phase microstructures were only obtained in CoCrFeMnNi at annealing temperatures ⩽700 °C [85], where Cr-rich phases were precipitated. As Cr was removed in the investigated alloy, the FCC phase was further stabilized.

The mechanical properties (Figs. 11,12) of CoFeMnNi showed a low hardness (156 HV0.1) combined with low strength (280 MPa $R_{p0.2}$ and 475 MPa R_m) and ductility (13 % A_g). Compared to CoCrFeMnNi MPEAs in recrystallized or PBF-LB condition [86,87], where ~300MPa $R_{p0.2}$, ~600 MPa R_m and ~50% A_g were obtained, CoFeMnNi showed lower strength and considerably lower elongation. The decrease in strength was caused by the removal of Cr, which was the only element in CoCrFeMnNi resulting in meaningful solid solution hardening due to a high lattice misfit compared to the other elements [88]. However, the large decrease in elongation is rather untypical for Cantor-type FCC MPEAs [4]. The CoCrFeMnNi alloy does usually show the activation of the twinning-induced plasticity (TWIP) effect during room temperature deformation [89] due to its relatively low SFE [90]. Hence, this effect promotes increased strain hardening resulting in the inhibition of local necking and thus enhanced elongation [42]. In our previous study [58], theoretical calculations revealed pure CoFeMnNi to have a strongly increased SFE compared to CoCrFeMnNi by about 30 mJ m^{-2}. This in combination with the observed strongly declining strain hardening rate during deformation (see Fig. 2a in the supplementary material) signify the suppression of TWIP activation [42]. Therefore, the high SFE in CoFeMnNi by the removal of Cr resulted in a poor strain hardening response and reduced ductility compared to CoCrFeMnNi.

4.2. Microstructure and properties of the $C_x(CoFeMnNi)_{100-x}$ system

Similar to the CoFeMnNi parent alloy, the investigated $Al^{0.0}C^x$ alloys were single-phase FCC (Figs. 2,3,5,6) at annealing temperatures ⩾550 °C. The FCC lattice parameter increased slightly by 0.002 Åat.%$^{-1}$ due to C in interstitial solution [55]. The removal of Cr successfully suppressed the formation of $M_{23}C_6$ carbides typically seen in C-added MPEAs of the CoCrFeMnNi system [43,14,44–54], even at low annealing temperatures of 550 °C. Therefore, the removal of Cr was effectively used to increase the C solubility in the FCC phase.

The mean hardness was increased from 156HV0.1 to 167 and 204HV0.1 in the $Al^{0.0}C^{0.8}$ and $Al^{0.0}C^{1.3}$ alloys, respectively (Fig. 11). C in solid solution increased the strength by 153 MPa at.%$^{-1}$ with slight yield strength increases (Figs. 12b,c), while simultaneously resulting in a strong elongation increase. Solid solution hardening by C coincides with hardness and strength increases in MPEAs due to a high lattice friction of stress of 184 MPa at.%$^{-1}$ [55], much higher than in conventional single-phase austenitic steels (e.g., high-Mn steel) [57]. Similar results were also obtained in the investigated CoFeMnNi alloy. However, another deformation mechanism must have been activated due to simultaneous higher tensile strength and elongation. The activation of TWIP is likely, but in our previous study [58] the addition of C to CoFeMnNi was predicted to result in higher SFE and, therefore, weakening or suppressing the TWIP effect. Nevertheless, a similar effect can be seen in austenitic steels, where the lack of C prevents TWIP activation, even though the SFE is low. The reason behind this is that solid solution strengthening by C and the formation of C–Mn clusters initiate TWIP due to a higher critical resolved shear stress [42,58] and increased stacking fault width due to dislocation pinning [91]. A similar effect may lead to the activation of TWIP in C-added CoFeMnNi. With the addition of C, the strain hardening behavior became similar to CoCrFeMnNi-type alloys [89,86,87] (see supplementary material), which typically show the activation of the TWIP effect. Therefore, the addition of C to CoFeMnNi resulted in TWIP activation and similar mechanical properties to CoCrFeMnNi alloys. C in solid solution was increased without Cr, but solid solution hardening by C only resulted in a small yield strength increase.

4.3. Microstructure and properties of the $Al_x(CoFeMnNi)_{100-x}$ system

At annealing temperatures ⩾700 °C, the addition of Al to CoFeMnNi resulted in the formation of BCC island- and plate-type phases (Fig. 8)) up to a dual-phase structure in the $Al^{22.1}C^{0.0}$ alloy (Fig. 7). Al was also found to some extent in solution of the FCC phase, where it increased the lattice parameter by 0.003 Åat.%$^{-1}$

due to its high lattice misfit [22,23]. The BCC phase had an average lattice parameter of 2.895 Å (Figs. 2 and 3), was enriched in Al and Ni (Figs. 7,8) and showed clear superlattice reflections for the B2 ordered BCC phase (Fig. 8k). The ideal $B2_{NiAl}$ crystal was reported with a lattice parameter of 2.887 Å [92], which was close to the measured value considering that Co, Fe and Mn were also in solution to an extent. Therefore, the BCC phase (island-, plate- and dual-phase-type) showed clear indications for $B2_{NiAl}$ ordering. The volume fraction of $B2_{NiAl}$ increased with lower annealing temperatures until 700 °Celsius (Fig. 3c). The formation of $B2_{NiAl}$ is also typically seen in Al-added MPEAs from the CoCrFeMnNi system [23,93] with similar phase morphologies. Large $B2_{NiAl}$ islands formed during homogenization at grain boundary triple points and plates were formed within the initial FCC matrix at 900 and 700 °C (see illustration in Fig. 12a).

At an annealing temperature of 550 °C, the addition of Al resulted in fine BCC plate-type precipitates in the FCC matrix (Figs. 4n,o,p and 9). The morphology was similar to the annealing between 900 and 700 °C, but much thinner plates were obtained at an average of 20 nm. Bcc phases with lattice parameters of 2.913 and 2.876 Å (Fig. 9d) were measured, one rich in Ni + Al (Fig. 9h) and another in Co + Fe (Fig. 9f). The ideal $B2_{NiAl}$ and $B2_{CoFe}$ phases were reported with lattice parameters of 2.887 Å [92] and 2.857 Å [94], respectively. The measured lattice parameters are higher than the ideal values as the other constituting elements are in solution. Compared to $B2_{NiAl}$, $B2_{CoFe}$ has comparatively weak superlattice reflections due to similar properties of the constituting atoms [95], which, therefore, cannot be fully resolved within bulk material. Other elements in solution of the phases further weaken the possibility to measure superlattice reflections. As the superlattice peaks for $B2_{NiAl}$ were clearly visible and considerably widened, the fine Ni + Al rich plates were a $B2_{NiAl}$ phase. Additionally, weak B2 superlattice reflections were found in the bulk material (Fig. 9l) belonging to both types of plates. Therefore, the Co + Fe rich BCC phase is likely an ordered $B2_{CoFe}$ phase. Both $B2_{NiAl}$ and $B2_{CoFe}$ were detected in Al-containing alloys at 550 °C by XRD with similar lattice parameters (Figs. 2,3) and were visible as fine plates in the microstructure (Figs. 4n to p). Both phases precipitated plate-like with an orientation relationship of $\{111\}_{fcc}\|\{110\}_{B2}$ and $\langle 011\rangle_{fcc}\|\langle 011\rangle_{B2}$ and a resulting misorientation of 45°. The best fit for the two lattices are the nucleation and growth of a stepped configuration of $\{111\}_{fcc}$ and $\{110\}_{B2}$ planes, which results in plate-type BCC precipitates in a FCC matrix [96,97]. According to Hall et al. [96], the lattice spacing d difference $\frac{d(\{111\}_{fcc})-d(\{110\}_{B2})}{d(\{110\}_{B2})}$ should be small at ~2.5%, which is the case for $B2_{NiAl}$ and $B2_{CoFe}$ at 2.4 and 3.4%, respectively. Therefore, $B2_{NiAl}$ and $B2_{CoFe}$ precipitates form in plates in the FCC microstructure. The observed orientation relationship is also similar to other B2-containing MPEAs [98]. Due to a reduced diffusion ability, the plate thickness decreased from 400 to 20nm with lower annealing temperatures. A nucleation on grain boundaries does not lead to the described structure, but it resulted in island-type phases due to incoherent FCC-B2 interfaces.

An increase in the volume fraction of the B2 phase (Fig. 3c) resulted in increased hardness (Fig. 11a), regardless of precipitation type. In other CoCrFeMnNi-type MPEAs, the formation of the $B2_{NiAl}$ phase was reported to coincide with an increase in strength due to the high hardness of the $B2_{NiAl}$ phase [93,22,23]. Compared to the fully FCC microstructure, the formation of island-type $B2_{NiAl}$ phase resulted in a slight decrease in elongation with similar strength (Figs. 12d,e). An increase in the volume fraction (Fig. 3) and a decrease in plate thickness of the B2 phases resulted in increased hardness (Fig. 11a) and strength (Figs. 12d to g). The $B2_{NiAl}$ phase does not deform in the tensile testing due to its high yield strength of 2000MPa [92]. Therefore, the strong and brittle $B2_{NiAl}$ phase cannot accommodate strain during deformation, which led to decreased elongation due to the island-type phase without affecting the strength. Furthermore, increased amounts or finer plate-type phases resulted in a reduction in elongation at similar tensile strength (Fig. 12f) and increased yield strength (Fig. 12g) up to fully brittle failure with extremely fine plates after annealing at 550°C. Compared to the yield strength of $B2_{NiAl}$ at 2000MPa, the yield strength of $B2_{CoFe}$ is much lower at ~300MPa [99] and, therefore, these plates deformed and did not cause early failure. The hard $B2_{NiAl}$ plate-type precipitates cannot deform plastically, and the deformation has to be accommodated by their rotation [100], requiring high amounts of geometrically necessary dislocations (GNDS). As the hardness difference between matrix and precipitates is high, voids are formed around the precipitates [100]. The alloy cannot accommodate the strain and premature failure was induced. After annealing at 550°C, high amounts of fine $B2_{NiAl}$ plates and, therefore, failure initiation points resulted in a brittle failure mode. Regarding the mechanical properties in room temperature tensile testing, the most stable precipitate morphology of plates combined with a soft FCC matrix containing hard $B2_{NiAl}$ precipitates was not an effective strengthening path for Al-added CoFeMnNi, resulting in small strength increases with a significant drop in ductility.

4.4. Microstructure and properties of the $Al_xC_y(CoFeMnNi)_{100-x-y}$ system

At annealing temperatures $\geqslant$700°C, the addition of up to 2.3at.%$^{-1}$ C to Al-added CoFeMnNi had little effect on the microstructure development compared to samples without C (see Section 4.3). The formation of $B2_{NiAl}$-type island- and plate-like phases was also observed (Figs. 5,6) and the volume fraction was not affected by the addition of C (Fig. 3c). Additionally, the lattice parameter of $B2_{NiAl}$ did not change significantly by the addition of C (Fig. 3b). Therefore, C was in solution in the FCC phase due to its known higher solubility of C [55] and $B2_{NiAl}$ hardly dissolved any C.

At an annealing temperature of 550°C, the FCC phase decomposed and the formation of basketweave-type precipitates was observed (Figs. 5k,l and 6l). An analysis for these types of precipitates (Fig. 10) revealed the microstructure to consist of an FCC matrix with M_7C_3-type carbide lamellae as well as $B2_{NiAl}$, $B2_{CoFe}$ and $L1_2$ phases. The $B2_{NiAl}$ island-type phase was clearly found with its superlattice reflections in SYXRD without considerable peak broadening. Additionally, a $B2_{CoFe}$ phase without clear superlattice reflections was found in the precipitates rich in Co + Fe (Figs. 10g,h) with a 2.874Å lattice parameter, similar to the Al-added alloy (see Section 4.3 for the detailed argumentation). The $B2_{NiAl}$ and $B2_{CoFe}$ phases were also found in the bulk material (Fig. 10o) with weak superlattice reflections due to a lower amount of ordering from the solution of the constituting elements. The M_7C_3 carbide was rich in Fe, C and especially Mn compared to the surrounding microstructure (Figs. 10d,e,f,i,j,k,l). The formation of M_7C_3 carbides is typically found at low temperature annealing in FCC-based steels with, according to Ernst et al. [101], needle-shaped morphology (similar to the here observed lamellae), where M typically represents (Cr, Fe, Mn). The formation of $B2_{NiAl}$ precipitates reduced the Ni content in the surrounding microstructure and increased the stability of M_7C_3 [101], likely inducing the formation of the phase with higher Al contents in CoFeMnNi. The formation of $L1_2$ precipitates with a lattice parameter of 3.658Å rich in Al + Ni were also found (Figs. 10d,g,h). In the Al-added Cantor systems, the formation of Ni_3Al with a $L1_2$ crystal structure was often observed after low temperature annealing [102]. The ideal lattice parameter of the phase was reported to be 3.567Å [103] with a high solubility of C with up to 5.8at.%, where it increased the lattice parameter strongly by ~0.01Åat.%$^{-1}$. In other Al-added Cantor-type alloys, the lattice parameter of Ni_3Al was often reported with even higher

values of ~3.582Å due to other elements in solution [102]. Therefore, the $L1_2$ phase was found to be a Ni_3Al phase, where the other constituting elements and C were in solution, causing a much higher lattice parameter. As $L1_2$ can dissolve high amounts of C, the phase is analogous to κ-carbides [104], where C atoms occupy the center of the unity cell. As Ni_3Al was more stable, the formation of $B2_{NiAl}$ was suppressed in the FCC matrix, and the SYXRD results showed a low amount of peak broadening for $B2_{NiAl}$ (Fig. 10d). Overall, the FCC phase decomposed to FCC + $B2_{CoFe}$+Ni_3Al + M_7C_3 after annealing at 550°C in Al- and C-added CoFeMnNi.

Regarding the mechanical properties of Al- and C-added CoFeMnNi, the FCC-based alloys showed only minor increases in hardness (Fig. 11) and yield strength (Fig. 12c) due to solid solution hardening by Al and especially C [55]. Additionally, the tensile strength and ductility increased strongly by the simultaneous addition of Al and C in FCC-based samples (Fig. 12b). Our previous limited characterization of this system [58] showed that C additions to AlCoFeMnNi result in decreased SFE and the activation of TWIP during deformation. The increase in strain hardening by TWIP (see also Fig. 2b in the supplementary material) and the corresponding inhibition of local necking results in high strength and ductility [42] in Al- and C-added FCC-based CoFeMnNi. In addition to the density reducing effect of Al, this MPEA system may show a potential for properties not seen in conventional alloys. Similar to the alloys without C, an increase of the $B2_{NiAl}$ phase at annealing temperatures $\geqslant$700°C resulted in minor increases in strength at the cost of ductility (see Figs. 11 and 12f,g and Section 4.3 for a more detailed analysis). After annealing at 550°C, large amounts of hard $B2_{NiAl}$ intermetallics [92] and M_7C_3 carbides [101] were obtained, which resulted in an extremely high hardness of up to 800HV0.1 (Fig. 11). Due to the precipitate's high hardness, they do not deform and cannot accommodate strain hardening. During elastic deformation in tensile testing, high amounts of GNDs form in the matrix around the particle from the high hardness difference [100], which ultimately leads to premature failure without plastic deformation, i.e. embrittlement (Fig. 12). These properties may enable an application as a highly wear resistant alloy [51].

5. Conclusions

The properties of alloys in the $Al_xC_y(CoFeMnNi)_{100-x-y}$ system were analyzed to reveal the microstructure evolution during annealing and mechanical properties to identify the potential of designing MPEAS in this system. The alloy system was chosen based on the widely investigated CoCrFeMnNi system, where Cr was removed to prevent the formation of $M_{23}C_6$ carbides. A custom CALPHAD database initially developed for the CoCrFeMnNi system was extended by Al and C and provided the basis for theoretical screening of the system. Samples with up to x = 22.1at.% and y = 2.3at.% were generated, heat treated and subsequently characterized in detail.

- The equiatomic CoFeMnNi alloy is a single-phase FCC alloy between 1150 and 550°C. Due to the removal of the BCC stabilizing Cr compared to the CoCrFeMnNi Cantor alloy, the FCC phase was stable in a larger temperature range. CoFeMnNi is a low strength alloy (280MPa $R_{p0.2}$ and 475MPa R_m) with low ductility (13% A_g), as the removal of Cr resulted in higher SFE and the suppression of TWIP.
- C-added equiatomic CoFeMnNi alloys were single-phase FCC alloys between 1150 and 550°C, where the absence of Cr suppressed carbide formation. The introduction of C–Mn clusters led to the activation of TWIP and similar tensile properties to that of CoCrFeMnNi, i.e., low strength and high ductility. Nevertheless, a high solid solution hardening potential of 153MPa at. %$^{-1}$ C was revealed due to a higher lattice friction stress than in conventional alloys.
- In Al-added equiatomic CoFeMnNi alloys, the FCC phase was gradually replaced by the $B2_{NiAl}$ ordered BCC phase. At $\geqslant$1050°C, $B2_{NiAl}$ nucleated at FCC grain boundaries with an island-morphology, leading to dual-phase microstructures at high Al contents. Between 900 and 550°C, plate-type precipitates formed due to a low $\{111\}_{fcc}$ and $\{110\}_{B2}$ lattice spacing difference of $B2_{NiAl}$ or $B2_{CoFe}$ (only at 550°C) in FCC with 2.4 and 3.4%, respectively. Moderate strength increases were obtained by $B2_{NiAl}$ precipitates, where the high strength difference between soft FCC and hard $B2_{NiAl}$ paired with plate-type precipitate morphology also resulted in strain accumulation on the tip of the plates. Consequently, premature failure was induced and a strong reduction in ductility or brittle failure was obtained at high volume fractions of nm-sized plates. The sole precipitation of B2 plates by Al addition was ineffective to improve the mechanical properties at room temperature.
- Simultaneous Al and C addition to equiatomic CoFeMnNi resulted in a strong SFE decrease and the activation of the TWIP effect promoted higher strength and ductility in the FCC based alloys. At annealing temperatures $\geqslant$700°C, similar microstructures and mechanical properties morphologies were found as without C addition. At 550°C, κ-carbides ($L1_2$ Ni_3Al enriched in C) replaced the precipitation of $B2_{NiAl}$, where additional $B2_{CoFe}$ and lamellar M_7C_3 resulted in high hardness and embrittlement. Regarding the mechanical properties, FCC-based Al- and C-added CoFeMnNi showed the highest potential in tensile testing due to a simultaneous increase in strength and ductility as well as density reduction.

6. CRediT authorship contribution statement

Fabian Kies: Conceptualization, Formal analysis, Investigation, Methodology, Visualization, Writing – original draft, Writing – review & editing. **Mehdi Noori:** Investigation, Writing – original draft. **Simon Ewald:** Investigation, Resources. **Johannes H. Schleifenbaum:** Conceptualization, Funding acquisition. **Bengt Hallstedt:** Conceptualization, Funding acquisition, Investigation, Writing – original draft, Writing – review & editing. **Christian Haase:** Conceptualization, Funding acquisition, Supervision, Writing – review & editing.

7. Data availability

The raw/processed data required to reproduce these findings cannot be shared at this time as the data also forms part of an ongoing study.

Declaration of Competing Interest

The authors declare that they have no known competing financial interests or personal relationships that could have appeared to influence the work reported in this paper.

Acknowledgments

Funded by the Deutsche Forschungsgemeinschaft (DFG, German Research Foundation) – 388166069 and 439900808, and by the RWTH Aachen Seed-Fund project OPSF406 – G:(DE-82)ZUK2-SF-OPSF406. Additionally, the authors would like to thank Zigan Xu and Wenwen Song for their support in SYXRD measurements.

Appendix A. Supplementary material

Supplementary data associated with this article can be found, in the online version, at https://doi.org/10.1016/j.matdes.2022.111368.

References

[1] B. Cantor, I.T. Chang, P. Knight, A.J. Vincent, Microstructural development in equiatomic multicomponent alloys, Mater. Sci. Eng. A 375–377 (1-2 SPEC. ISS.) (2004) 213–218, doi: 10.1016/j.msea.2003.10.257, ISSN 09215093.

[2] J.W. Yeh, S.K. Chen, S.J. Lin, J.Y. Gan, T.S. Chin, T.T. Shun, C.H. Tsau, S.Y. Chang, Nanostructured high-entropy alloys with multiple principal elements: Novel alloy design concepts and outcomes, Adv. Eng. Mater. 6 (5) (2004), https://doi.org/10.1002/adem.200300567. pp. 299–303+274, ISSN 14381656.

[3] D.B. Miracle, O.N. Senkov, A critical review of high entropy alloys and related concepts, Acta Mater. 122 (2017) 448–511, https://doi.org/10.1016/j.actamat.2016.08.081. ISSN 13596454.

[4] E.P. George, W.A. Curtin, C.C. Tasan, High entropy alloys: A focused review of mechanical properties and deformation mechanisms, Acta Mater. 188 (2020) 435–474, https://doi.org/10.1016/j.actamat.2019.12.015. ISSN 13596454.

[5] J. Chen, X. Zhou, W. Wang, B. Liu, Y. Lv, W. Yang, D. Xu, Y. Liu, A review on fundamental of high entropy alloys with promising high–temperature properties, J. Alloy. Compd. 760 (2018) 15–30, https://doi.org/10.1016/j.jallcom.2018.05.067. ISSN 09258388.

[6] M.H. Tsai, J.W. Yeh, High-entropy alloys: A critical review, Mater. Res. Lett. 2 (3) (2014) 107–123, https://doi.org/10.1080/21663831.2014.912690. ISSN 21663831.

[7] T. Borkar, B. Gwalani, D. Choudhuri, C.V. Mikler, C.J. Yannetta, X. Chen, R.V. Ramanujan, M.J. Styles, M.A. Gibson, R. Banerjee, A combinatorial assessment of AlxCrCuFeNi2 (0 <x <1.5) complex concentrated alloys: Microstructure, microhardness, and magnetic properties, Acta Mater. 116 (2016) 63–76, https://doi.org/10.1016/j.actamat.2016.06.025. ISSN 1359-6454.

[8] K.R. Lim, K.S. Lee, J.S. Lee, J.Y. Kim, H.J. Chang, Y.S. Na, Dual-phase high-entropy alloys for high-temperature structural applications, J. Alloy. Compd. 728 (2017) 1235–1238, https://doi.org/10.1016/j.jallcom.2017.09.089. ISSN 09258388.

[9] E.P. George, D. Raabe, R.O. Ritchie, High-entropy alloys, Nat. Rev. Mater. 4 (8) (2019) 515–534, https://doi.org/10.1038/s41578-019-0121-4. ISSN 20588437.

[10] Y. Ye, Q. Wang, J. Lu, C. Liu, Y. Yang, High-entropy alloy: challenges and prospects, Mater. Today 19 (6) (2016) 349–362, https://doi.org/10.1016/j.mattod.2015.11.026. ISSN 13697021.

[11] F. Otto, A. Dlouhý, C. Somsen, H. Bei, G. Eggeler, E.P. George, The influences of temperature and microstructure on the tensile properties of a CoCrFeMnNi high-entropy alloy, Acta Mater. 61 (15) (2013) 5743–5755, https://doi.org/10.1016/j.actamat.2013.06.018. ISSN 13596454.

[12] R. Chen, G. Qin, H. Zheng, L. Wang, Y. Su, Y.L. Chiu, H. Ding, J. Guo, H. Fu, Composition design of high entropy alloys using the valence electron concentration to balance strength and ductility, Acta Mater. 144 (2018) 129–137, https://doi.org/10.1016/j.actamat.2017.10.058. ISSN 13596454.

[13] J.C. Rao, H.Y. Diao, V. Ocelík, D. Vainchtein, C. Zhang, C. Kuo, Z. Tang, W. Guo, J. D. Poplawsky, Y. Zhou, P.K. Liaw, J.T.M. De Hosson, Secondary phases in Al x CoCrFeNi high-entropy alloys: An in-situ TEM heating study and thermodynamic appraisal, Acta Mater. 131 (2017) 206–220, https://doi.org/10.1016/j.actamat.2017.03.066. ISSN 13596454.

[14] N.D. Stepanov, N.Y. Yurchenko, M.A. Tikhonovsky, G.A. Salishchev, Effect of carbon content and annealing on structure and hardness of the CoCrFeNiMn-based high entropy alloys, J. Alloy. Compd. 687 (2016) 59–71, https://doi.org/10.1016/j.jallcom.2016.06.103.

[15] Y. Tan, J. Li, J. Wang, M. Kolbe, H. Kou, Microstructure characterization of CoCrFeNiMnPdx eutectic high-entropy alloys, J. Alloy. Compd. 731 (2018) 600–611, https://doi.org/10.1016/j.jallcom.2017.09.057. ISSN 09258388.

[16] Z. Tang, M.C. Gao, H. Diao, T. Yang, J. Liu, T. Zuo, Y. Zhang, Z. Lu, Y. Cheng, Y. Zhang, K.A. Dahmen, P.K. Liaw, T. Egami, Aluminum alloying effects on lattice types, microstructures, and mechanical behavior of high-entropy alloys systems, Jom 65 (12) (2013) 1848–1858, https://doi.org/10.1007/s11837-013-0776-z. ISSN 10474838.

[17] B.S. Li, Y.P. Wang, M.X. Ren, C. Yang, H.Z. Fu, Effects of Mn, Ti and V on the microstructure and properties of AlCrFeCoNiCu high entropy alloy, Mater. Sci. Eng., A 498 (1–2) (2008) 482–486, https://doi.org/10.1016/j.msea.2008.08.025. ISSN 09215093.

[18] J.M. Zhu, H.M. Fu, H.F. Zhang, A.M. Wang, H. Li, Z.Q. Hu, Microstructures and compressive properties of multicomponent AlCoCrFeNiMo x alloys, Mater. Sci. Eng., A 527 (26) (2010) 6975–6979, https://doi.org/10.1016/j.msea.2010.07.028. ISSN 09215093.

[19] W. Huo, H. Zhou, F. Fang, X. Zhou, Z. Xie, J. Jiang, Microstructure and properties of novel CoCrFeNiTa x eutectic high-entropy alloys, J. Alloy. Compd. 735 (2018) 897–904, https://doi.org/10.1016/j.jallcom.2017.11.075. ISSN 09258388.

[20] P.E. Rivera-Díaz-Del-Castillo, H. Fu, Strengthening mechanisms in high-entropy alloys: Perspectives for alloy design, J. Mater. Res. 33 (19) (2018) 2970–2982, https://doi.org/10.1557/jmr.2018.328. ISSN 20445326.

[21] N.Y. Yurchenko, N.D. Stepanov, A.O. Gridneva, M.V. Mishunin, G.A. Salishchev, S.V. Zherebtsov, Effect of Cr and Zr on phase stability of refractory Al-Cr-Nb-Ti-V-Zr high-entropy alloys, J. Alloy. Compd. 757 (2018) 403–414, https://doi.org/10.1016/j.jallcom.2018.05.099. ISSN 09258388.

[22] J. Kumar, N. Kumar, S. Das, N.P. Gurao, K. Biswas, Effect of Al Addition on the Microstructural Evolution of Equiatomic CoCrFeMnNi Alloy, Trans. Indian Inst. Met. 71 (11) (2018) 2749–2758, https://doi.org/10.1007/s12666-018-1443-4. ISSN 09751645.

[23] J.Y. He, W.H. Liu, H. Wang, Y. Wu, X.J. Liu, T.G. Nieh, Z.P. Lu, Effects of Al addition on structural evolution and tensile properties of the FeCoNiCrMn high-entropy alloy system, Acta Mater. 62 (1) (2014) 105–113, https://doi.org/10.1016/j.actamat.2013.09.037. ISSN 13596454.

[24] Y.F. Kao, T.J. Chen, S.K. Chen, J.W. Yeh, Microstructure and mechanical property of as-cast, -homogenized, and -deformed AlxCoCrFeNi high-entropy alloys, J. Alloy. Compd. 488 (1) (2009) 57–64, https://doi.org/10.1016/j.jallcom.2009.08.090. ISSN 09258388.

[25] H.P. Chou, Y.S. Chang, S.K. Chen, J.W. Yeh, Microstructure, thermophysical and electrical properties in AlxCoCrFeNi high-entropy alloys, Materials Science and Engineering B: Solid-State Materials for Advanced Technology 163 (3) (2009) 184–189, https://doi.org/10.1016/j.mseb.2009.05.024. ISSN 09215107.

[26] J. Cieslak, J. Tobola, K. Berent, M. Marciszko, Phase composition of Al x FeNiCrCo high entropy alloys prepared by sintering and arc-melting methods, J. Alloy. Compd. 740 (2018) 264–272, https://doi.org/10.1016/j.jallcom.2017.12.333. ISSN 09258388.

[27] J. Joseph, T. Jarvis, X. Wu, N. Stanford, P. Hodgson, D.M. Fabijanic, Comparative study of the microstructures and mechanical properties of direct laser fabricated and arc-melted AlxCoCrFeNi high entropy alloys, Mater. Sci. Eng., A 633 (2015) 184–193, https://doi.org/10.1016/j.msea.2015.02.072. ISSN 09215093.

[28] C. Li, J.C. Li, M. Zhao, Q. Jiang, Effect of aluminum contents on microstructure and properties of Al xCoCrFeNi alloys, J. Alloy. Compd. 504 (SUPPL. 1) (2010) S515–S518, https://doi.org/10.1016/j.jallcom.2010.03.111. ISSN 09258388.

[29] M. Li, J. Gazquez, A. Borisevich, R. Mishra, K.M. Flores, Evaluation of microstructure and mechanical property variations in AlxCoCrFeNi high entropy alloys produced by a high-throughput laser deposition method, Intermetallics 95 (2018) 110–118, https://doi.org/10.1016/j.intermet.2018.01.021. ISSN 09669795.

[30] W.R. Wang, W.L. Wang, S.C. Wang, Y.C. Tsai, C.H. Lai, J.W. Yeh, Effects of Al addition on the microstructure and mechanical property of Al xCoCrFeNi high-entropy alloys, Intermetallics 26 (2012) 44–51, https://doi.org/10.1016/j.intermet.2012.03.005. ISSN 09669795.

[31] T. Yang, S. Xia, S.S.S.S. Liu, C. Wang, S.S.S.S. Liu, Y. Zhang, J. Xue, S. Yan, Y. Wang, Effects of AL addition on microstructure and mechanical properties of AlxCoCrFeNi High-entropy alloy, Mater. Sci. Eng., A 648 (2015) 15–22, https://doi.org/10.1016/j.msea.2015.09.034. ISSN 09215093.

[32] K. Masemola, N. Malatji, A. Patricia Popoola, Evaluation of microstructural and mechanical properties of AlxCrFeMnNi high entropy alloys, Materials Today: Proceedings 28 (2019) 898–901, doi: 10.1016/j.matpr.2019.12.320, ISSN 22147853.

[33] E.G. Astafurova, K.A. Reunova, E.V. Melnikov, M.Y. Panchenko, S.V. Astafurov, G.G. Maier, V.A. Moskvina, On the difference in carbon- and nitrogen-alloying of equiatomic FeMnCrNiCo high-entropy alloy, Mater. Lett. 276 (2020) 128183, https://doi.org/10.1016/j.matlet.2020.128183. ISSN 18734979.

[34] W. Zhang, D. Yan, W. Lu, Z. Li, Carbon and nitrogen co-doping enhances phase stability and mechanical properties of a metastable high-entropy alloy, J. Alloy. Compd. 831 (2020) 154799, https://doi.org/10.1016/j.jallcom.2020.154799.

[35] H. Kwon, J. Moon, J.W. Bae, J.M. Park, S. Son, H.S. Do, B.J. Lee, H.S. Kim, Precipitation-driven metastability engineering of carbon-doped CoCrFeNiMo medium-entropy alloys at cryogenic temperature, Scripta Mater. 188 (2020) 140–145, https://doi.org/10.1016/j.scriptamat.2020.07.023. ISSN 13596462.

[36] M. Klimova, D. Shaysultanov, A. Semenyuk, S. Zherebtsov, G. Salishchev, N. Stepanov, Effect of nitrogen on mechanical properties of CoCrFeMnNi high entropy alloy at room and cryogenic temperatures, J. Alloy. Compd. 849 (2020) 156633, https://doi.org/10.1016/j.jallcom.2020.156633. ISSN 09258388.

[37] I. Moravcik, J. Cizek, L.d.A. Gouvea, J. Cupera, I. Guban, I. Dlouhy, Nitrogen interstitial alloying of CoCrFeMnNi high entropy alloy through reactive powder milling, Entropy 21 (4) (2019) 1–7, https://doi.org/10.3390/e21040363. ISSN 10994300.

[38] M. Song, R. Zhou, J. Gu, Z. Wang, S. Ni, Y. Liu, Nitrogen induced heterogeneous structures overcome strength-ductility trade-off in an additively manufactured high-entropy alloy, Applied Materials Today 18 (2020) 1–6, https://doi.org/10.1016/j.apmt.2019.100498. ISSN 23529407.

[39] D.E. Jodi, J. Park, N. Park, Strengthening of ultrafine-grained equiatomic CoCrFeMnNi high-entropy alloy by nitrogen addition, Mater. Lett. 258 (2020) 126772, https://doi.org/10.1016/j.matlet.2019.126772. ISSN 18734979.

[40] J.B. Seol, J.W. Bae, Z. Li, J. Chan Han, J.G. Kim, D. Raabe, H.S. Kim, Boron doped ultrastrong and ductile high-entropy alloys, Acta Materialia, doi: 10.1016/j.actamat.2018.04.004, ISSN 13596454.

[41] C. Haase, C. Zehnder, T. Ingendahl, A. Bikar, F. Tang, B. Hallstedt, W. Hu, W. Bleck, D.A. Molodov, On the deformation behavior of κ-carbide-free and κ-carbide-containing high-Mn light-weight steel, Acta Mater. 122 (2017) 332–343, https://doi.org/10.1016/j.actamat.2016.10.006. ISSN 13596454.

[42] B.C. De Cooman, Y. Estrin, S.K. Kim, Twinning-induced plasticity (TWIP) steels, Acta Mater. 142 (2018) 283–362, https://doi.org/10.1016/j.actamat.2017.06.046. ISSN 13596454.
[43] W.F. Wu, N. Gao, X.W. Liu, W. Guo, L. Yang, Z.T. Fan, Precipitation behavior of carbides in a low-carbon NiCoFeCr high-entropy alloy at 800 C, Mater. Lett. 298 (2021) 1–4, https://doi.org/10.1016/j.matlet.2021.130020. ISSN 18734979.
[44] J.Y. Ko, S.I. Hong, Microstructural evolution and mechanical performance of carbon-containing CoCrFeMnNi-C high entropy alloys, J. Alloy. Compd. 743 (2018) 115–125, https://doi.org/10.1016/j.jallcom.2018.01.348.
[45] J.Y. Ko, J.S. Song, S.I. Hong, Effect of Carbon Addition and Recrystallization on the Microstructure and Mechanical Properties of CoCrFeMnNi High Entropy Alloys, Korean Journal of Metals and Materials 56 (1) (2018) 26–33, https://doi.org/10.3365/KJMM.2018.56.1.26. ISSN 82428217.
[46] N.D. Stepanov, D.G. Shaysultanov, R.S. Chernichenko, N.Y. Yurchenko, S.V. Zherebtsov, M.A. Tikhonovsky, G.A. Salishchev, Effect of thermomechanical processing on microstructure and mechanical properties of the carbon-containing CoCrFeNiMn high entropy alloy, J. Alloy. Compd. 693 (2017) 394–405, https://doi.org/10.1016/j.jallcom.2016.09.208. ISSN 09258388.
[47] Z. Wu, C.M. Parish, H. Bei, Nano-twin mediated plasticity in carbon-containing FeNiCoCrMn high entropy alloys, J. Alloy. Compd. 647 (2015) 815–822, https://doi.org/10.1016/j.jallcom.2015.05.224.
[48] J. Peng, Z. Li, L. Fu, X. Ji, Z. Pang, A. Shan, Carbide precipitation strengthening in fine-grained carbon-doped FeCoCrNiMn high entropy alloy, J. Alloy. Compd. 803 (2019) 491–498, https://doi.org/10.1016/j.jallcom.2019.06.204. ISSN 09258388.
[49] J.M. Park, J. Choe, J.G. Kim, J.W. Bae, J. Moon, S. Yang, K.T. Kim, J.-H. Yu, H.S. Kim, Superior tensile properties of 1%C-CoCrFeMnNi high-entropy alloy additively manufactured by selective laser melting, Materials Research Letters 8 (1) (2020) 1–7, https://doi.org/10.1080/21663831.2019.1638844. ISSN null.
[50] Q.-J. Li, H. Sheng, E. Ma, Strengthening in multi-principal element alloys with local-chemical-order roughened dislocation pathways, Nature Communications 10 (1) (2019) 3563, https://doi.org/10.1038/s41467-019-11464-7. ISSN 2041-1723.
[51] J.-K. Xiao, H. Tan, J. Chen, A. Martini, C. Zhang, Effect of carbon content on microstructure, hardness and wear resistance of CoCrFeMnNiCx high-entropy alloys, J. Alloy. Compd. 847 (2020) 156533, https://doi.org/10.1016/j.jallcom.2020.156533.
[52] L.B. Chen, R. Wei, K. Tang, J. Zhang, F. Jiang, L. He, J. Sun, Heavy carbon alloyed FCC-structured high entropy alloy with excellent combination of strength and ductility, Mater. Sci. Eng., A 716 (January) (2018) 150–156, https://doi.org/10.1016/j.msea.2018.01.045.
[53] X.W. Liu, L. Liu, G. Liu, X.X. Wu, D.H. Lu, J.Q. Yao, W.M. Jiang, Z.T. Fan, W.B. Zhang, The Role of Carbon in Grain Refinement of Cast CrFeCoNi High-Entropy Alloys, Metallurgical and Materials Transactions A 49 (6) (2018) 2151–2160, https://doi.org/10.1007/s11661-018-4549-8.
[54] R. Zhou, Y. Liu, B. Liu, J. Li, Q. Fang, Precipitation behavior of selective laser melted FeCoCrNiC 0.05 high entropy alloy, Intermetallics 106 (2019) 20–25, https://doi.org/10.1016/j.intermet.2018.12.001. ISSN 09669795.
[55] Z. Wang, I. Baker, Z. Cai, S. Chen, J.D. Poplawsky, W. Guo, The effect of interstitial carbon on the mechanical properties and dislocation substructure evolution in Fe40.4Ni11.3Mn34.8Al7.5Cr6high entropy alloys, Acta Mater. 120 (2016) 228–239, https://doi.org/10.1016/j.actamat.2016.08.072. ISSN 1359-6454.
[56] E. Astafurova, E. Melnikov, S. Astafurov, K. Reunova, M. Panchenko, V. Moskvina, I. Tumbusova, A comparative study of a solid solution hardening in carbon-alloyed FeMnCrNiCo0.95C0.05 high-entropy alloy subjected to different thermal–mechanical treatments, Materials Letters 285 (2021) 129073, doi: 10.1016/j.matlet.2020.129073, ISSN 18734979.
[57] O. Bouaziz, H. Zurob, B. Chehab, J.D. Embury, S. Allain, M. Huang, Effect of chemical composition on work hardening of Fe—Mn—C TWIP steels, Mater. Sci. Technol. 27 (3) (2011) 707–709, https://doi.org/10.1179/026708309X12535382371852. ISSN 0267-0836.
[58] F. Kies, Y. Ikeda, S. Ewald, J.H. Schleifenbaum, B. Hallstedt, F. Körmann, C. Haase, Combined Al and C alloying enables mechanism-oriented design of multi-principal element alloys: Ab initio calculations and experiments, Scripta Mater. 178 (2020) 366–371, https://doi.org/10.1016/j.scriptamat.2019.12.004. ISSN 1359-6462.
[59] F. Kies, X. Wu, B. Hallstedt, Z. Li, C. Haase, Enhanced precipitation strengthening of multi-principal element alloys by κ- and B2-phases, Materials & Design 198 (2021) 109315, https://doi.org/10.1016/j.matdes.2020.109315. ISSN 0264-1275.
[60] H. Lukas, S. Fries, B. Sundman, Computational thermodynamics. The CALPHAD method, Cambridge University Press, Cambridge, 2007, https://doi.org/10.1088/0305-4470/27/7/011. ISBN 978-0-521-86811-2.
[61] N. Saunders, A. Miodownik, CALPHAD (calculation of phase diagrams). A comprehensive guide, Pergamon, New York, 1998. ISBN 0-08-042129-6.
[62] M. Detrois, S. Antonov, S. Tin, Phase stability and thermodynamic database validation in a set of non-equiatomic Al-Co-Cr-Fe-Nb-Ni high-entropy alloys, Intermetallics 104 (2019) 103–112, https://doi.org/10.1016/j.intermet.2018.11.002. ISSN 09669795.
[63] T. Nagase, M. Takemura, M. Matsumuro, T. Maruyama, Solidification microstructure of AlCoCrFeNi2.1 eutectic high entropy alloy ingots, Mater. Trans. 59 (2) (2018) 255–264, https://doi.org/10.2320/matertrans.F-M2017851. ISSN 13459678.
[64] O.N. Senkov, J.D. Miller, D.B. Miracle, C. Woodward, Accelerated exploration of multi-principal element alloys for structural applications, Calphad: Computer Coupling of Phase Diagrams and Thermochemistry 50 (2015) 32–48, doi: 10.1016/j.calphad.2015.04.009, ISSN 03645916.
[65] M. Gao, D. Alman, Searching for Next Single-Phase High-Entropy Alloy Compositions, Entropy 15 (10) (2013) 4504–4519, https://doi.org/10.3390/e15104504. ISSN 1099-4300.
[66] C. Haase, F. Tang, M.B. Wilms, A. Weisheit, B. Hallstedt, Combining thermodynamic modeling and 3D printing of elemental powder blends for high-throughput investigation of high-entropy alloys – Towards rapid alloy screening and design, Mater. Sci. Eng., A 688 (January) (2017) 180–189, https://doi.org/10.1016/j.msea.2017.01.099. ISSN 09215093.
[67] S. Ewald, F. Kies, S. Hermsen, M. Voshage, C. Haase, J.H. Schleifenbaum, Rapid Alloy Development of Extremely High-Alloyed Metals Using Powder Blends in Laser Powder Bed Fusion, Materials 12 (10) (2019) 1706, https://doi.org/10.3390/ma12101706. ISSN 1996-1944.
[68] J.O. Andersson, T. Helander, L. Höglund, P. Shi, B. Sundman, Thermo-Calc & DICTRA, computational tools for materials science, Calphad: Computer Coupling of Phase Diagrams and Thermochemistry 26 (2) (2002) 273–312, doi: 10.1016/S0364-5916(02)00037-8, ISSN 03645916.
[69] T. DebRoy, H.L. Wei, J.S. Zuback, T. Mukherjee, J.W. Elmer, J.O. Milewski, A.M. Beese, A. Wilson-Heid, A. De, W. Zhang, Additive manufacturing of metallic components – Process, structure and properties, Prog. Mater Sci. 92 (2018) 112–224, https://doi.org/10.1016/j.pmatsci.2017.10.001. ISSN 00796425.
[70] F. Kies, M.B. Wilms, N. Pirch, K.G. Pradeep, J.H. Schleifenbaum, C. Haase, Defect formation and prevention in directed energy deposition of high-manganese steels and the effect on mechanical properties, Materials Science and Engineering: A 772 (2020) 138688, https://doi.org/10.1016/j.msea.2019.138688. ISSN 0921-5093.
[71] M.D. Sangid, T.A. Book, D. Naragani, J. Rotella, P. Ravi, A. Finch, P. Kenesei, J.-S. Park, H. Sharma, J. Almer, X. Xiao, Role of heat treatment and build orientation in the microstructure sensitive deformation characteristics of IN718 produced via SLM additive manufacturing, Additive Manufacturing 22 (2018) 479–496, https://doi.org/10.1016/j.addma.2018.04.032. ISSN 2214-8604.
[72] S. Cheruvathur, E.A. Lass, C.E. Campbell, Additive Manufacturing of 17–4 PH Stainless Steel: Post-processing Heat Treatment to Achieve Uniform Reproducible Microstructure, JOM 68 (3) (2016) 930–942, https://doi.org/10.1007/s11837-015-1754-4. ISSN 1543-1851.
[73] N. Oono, K. Nakamura, S. Ukai, T. Kaito, T. Torimaru, A. Kimura, S. Hayashi, Oxide particle coarsening at temperature over 1473 K in 9CrODS steel, Nuclear Materials and Energy 9 (2016) 342–345, https://doi.org/10.1016/j.nme.2016.06.008. ISSN 23521791.
[74] P. Zheng, Y. Li, J. Zhang, J. Shen, T. Nagasaka, T. Muroga, H. Abe, On the thermal stability of a 9Cr-ODS steel aged at 700 C up to 10000 h - Mechanical properties and microstructure, Materials Science and Engineering: A 783 (2020) 139292, https://doi.org/10.1016/j.msea.2020.139292. ISSN 0921-5093.
[75] D. Riabov, M. Rashidi, E. Hryha, S. Bengtsson, Effect of the powder feedstock on the oxide dispersion strengthening of 316L stainless steel produced by laser powder bed fusion, Mater. Charact. 169 (2020) 110582, https://doi.org/10.1016/j.matchar.2020.110582. ISSN 1044-5803.
[76] F. Kies, P. Köhnen, M.B. Wilms, F. Brasche, K.G. Pradeep, A. Schwedt, S. Richter, A. Weisheit, J.H. Schleifenbaum, C. Haase, Design of high-manganese steels for additive manufacturing applications with energy-absorption functionality, Materials & Design 160 (2018) 1250–1264, https://doi.org/10.1016/j.matdes.2018.10.051. ISSN 0264-1275.
[77] F. Bachmann, R. Hielscher, H. Schaeben, Grain detection from 2d and 3d EBSD data-Specification of the MTEX algorithm, Ultramicroscopy 111 (12) (2011) 1720–1733, https://doi.org/10.1016/j.ultramic.2011.08.002. ISSN 03043991.
[78] G. Nolze, R. Hielscher, Orientations – perfectly colored, J. Appl. Crystallogr. 49 (5) (2016) 1786–1802, https://doi.org/10.1107/s1600576716012942. ISSN 1600-5767.
[79] P. Stadelmann, Image analysis and simulation software in transmission electron microscopy, Microsc. Microanal. 9 (S03) (2003) 60–61, https://doi.org/10.1017/S1431927603012224. ISSN 1431-9276, 1435-8115.
[80] A.P. Hammersley, FIT2D: An Introduction and Overview, ESRF Internal Report ESRF97HA02.
[81] A.P. Hammersley, S.O. Svensson, M. Hanfland, A.N. Fitch, D. Hausermann, Two-dimensional detector software: From real detector to idealised image or two-theta scan, High Pressure Research 14 (4–6) (2007) 235–248, https://doi.org/10.1080/08957959608201408. ISSN 0895-7959.
[82] M. Ferrari, L. Lutterotti, Method for the simultaneous determination of anisotropic residual stresses and texture by x-ray diffraction, J. Appl. Phys. 76 (11) (1994) 7246–7255, https://doi.org/10.1063/1.358006. ISSN 00218979.
[83] V.S. Hariharan, A. Karati, T. Parida, R. John, D.A. Babu, B.S. Murty, Effect of Al addition and homogenization treatment on the magnetic properties of CoFeMnNi high-entropy alloy, J. Mater. Sci. 55 (36) (2020) 17204–17217, https://doi.org/10.1007/s10853-020-05171-8. ISSN 1573-4803.
[84] P. Cui, Y. Ma, L. Zhang, M. Zhang, J. Fan, W. Dong, P. Yu, G. Li, R. Liu, Effect of Ti on microstructures and mechanical properties of high entropy alloys based on CoFeMnNi system, Materials Science and Engineering: A 737 (2018) 198–204, https://doi.org/10.1016/j.msea.2018.09.050. ISSN 0921-5093.
[85] F. Otto, A. Dlouhý, K.G. Pradeep, M. Kuběnová, D. Raabe, G. Eggeler, E.P. George, Decomposition of the single-phase high-entropy alloy CrMnFeCoNi after prolonged anneals at intermediate temperatures, Acta Mater. 112

(2016) 40–52, https://doi.org/10.1016/j.actamat.2016.04.005. ISSN 13596454.
[86] Z.G. Zhu, Q.B. Nguyen, F.L. Ng, X.H. An, X.Z. Liao, P.K. Liaw, S.M.L. Nai, J. Wei, Hierarchical microstructure and strengthening mechanisms of a CoCrFeNiMn high entropy alloy additively manufactured by selective laser melting, Scripta Mater. 154 (2018) 20–24, https://doi.org/10.1016/j.scriptamat.2018.05.015. ISSN 1359-6462.
[87] R. Li, P. Niu, T. Yuan, P. Cao, C. Chen, K. Zhou, Selective laser melting of an equiatomic CoCrFeMnNi high-entropy alloy: Processability, non-equilibrium microstructure and mechanical property, J. Alloy. Compd. 746 (2018) 125–134, https://doi.org/10.1016/j.jallcom.2018.02.298. ISSN 0925-8388.
[88] Z. Wu, H. Bei, F. Otto, G.M. Pharr, E.P. George, Recovery, recrystallization, grain growth and phase stability of a family of FCC-structured multi-component equiatomic solid solution alloys, Intermetallics 46 (2014) 131–140, https://doi.org/10.1016/j.intermet.2013.10.024. ISSN 09669795.
[89] J.H. Kim, K.R. Lim, J.W. Won, Y.S. Na, H.S. Kim, Mechanical properties and deformation twinning behavior of as-cast CoCrFeMnNi high-entropy alloy at low and high temperatures, Materials Science and Engineering A 712 (October 2017) (2018) 108–113, doi: 10.1016/j.msea.2017.11.081, ISSN 09215093.
[90] Y. Ikeda, B. Grabowski, F. Körmann, Ab initio phase stabilities and mechanical properties of multicomponent alloys: A comprehensive review for high entropy alloys and compositionally complex alloys, Mater. Charact. 147 (2019) 464–511, https://doi.org/10.1016/j.matchar.2018.06.019. ISSN 10445803.
[91] S. Sevsek, F. Brasche, C. Haase, W. Bleck, Combined deformation twinning and short-range ordering causes serrated flow in high-manganese steels, Mater. Sci. Eng., A 746 (2019) 434–442, https://doi.org/10.1016/j.msea.2019.01.042. ISSN 09215093.
[92] R.D. Noebe, R.R. Bowman, M.V. Nathal, Physical and mechanical properties of the B2 compound NiAl, Int. Mater. Rev. 38 (4) (1993) 193–232, https://doi.org/10.1179/imr.1993.38.4.193. ISSN 0950-6608.
[93] M. Aizenshtein, E. Priel, S. Hayun, Effect of pre-deformation and B2 morphology on the mechanical properties of Al0.5CoCrFeNi HEA, Materials Science and Engineering: A 788 (2020) 139575, https://doi.org/10.1016/j.msea.2020.139575. ISSN 0921-5093.
[94] T. Nishizawa, K. Ishida, The Co-Fe (Cobalt-Iron) system, Bulletin of Alloy Phase Diagrams 5 (3) (1984) 250, https://doi.org/10.1007/BF02868548. ISSN 0197-0216.
[95] D.W. Clegg, R.A. Buckley, The Disorder Order Transformation in Iron–Cobalt-Based Alloys, Metal Science Journal 7 (1) (1973) 48–54, https://doi.org/10.1179/030634573790445541. ISSN 0026-0681.
[96] M.G. Hall, H.I. Aaronson, K.R. Kinsma, The structure of nearly coherent fcc: bcc boundaries in a Cu-Cr alloy, Surf. Sci. 31 (1972) 257–274, https://doi.org/10.1016/0039-6028(72)90264-6. ISSN 0039-6028.
[97] G.C. Weatherly, W.Z. Zhang, The invariant line and precipitate morphology in Fcc-Bcc systems, Metallurgical and Materials Transactions A 25 (9) (1994) 1865–1874, https://doi.org/10.1007/BF02649034. ISSN 1073-5623, 1543-1940.
[98] J.C. Rao, V. Ocelík, D. Vainchtein, Z. Tang, P.K. Liaw, J.T.M. De Hosson, The fcc-bcc crystallographic orientation relationship in AlxCoCrFeNi high-entropy alloys, Mater. Lett. 176 (2016) 29–32, https://doi.org/10.1016/j.matlet.2016.04.086. ISSN 18734979.
[99] N.S. Stoloff, R.G. Davies, The plastic deformation of ordered FeCo and Fe3 Al alloys, Acta Metall. 12 (5) (1964) 473–485, https://doi.org/10.1016/0001-6160(64)90019-7. ISSN 0001-6160.
[100] S.P. Yuan, R.H. Wang, G. Liu, R. Li, J.M. Park, J. Sun, K.H. Chen, Effects of precipitate morphology on the notch sensitivity of ductile fracture in heat-treatable aluminum alloys, Materials Science and Engineering: A 527 (27) (2010) 7369–7381, https://doi.org/10.1016/j.msea.2010.07.103. ISSN 0921-5093.
[101] F. Ernst, D. Li, H. Kahn, G.M. Michal, A.H. Heuer, The carbide M7C3 in low-temperature-carburized austenitic stainless steel, Acta Mater. 59 (6) (2011) 2268–2276, https://doi.org/10.1016/j.actamat.2010.11.058. ISSN 1359-6454.
[102] Y.J. Liang, L. Wang, Y. Wen, B. Cheng, Q. Wu, T. Cao, Q. Xiao, Y. Xue, G. Sha, Y. Wang, Y. Ren, X. Li, L. Wang, F. Wang, H. Cai, High-content ductile coherent nanoprecipitates achieve ultrastrong high-entropy alloys, Nature Communications 9 (1) (2018) 4063, https://doi.org/10.1038/s41467-018-06600-8. ISSN 20411723.
[103] S.C. Huang, C.L. Briant, K.-M. Chang, A.I. Taub, E.L. Hall, Carbon effects in rapidly solidified Ni3Al, J. Mater. Res. 1 (1) (1986) 60–67, https://doi.org/10.1557/JMR.1986.0060. ISSN 2044-5326, 0884-2914.
[104] J. Xing, Y. Wei, L. Hou, An Overview of the Effects of Alloying Elements on the Properties of Lightweight Fe-(15–35) Mn-(5–12) Al-(0.3–1.2) C Steel, Jom 70 (6) (2018) 929–937, https://doi.org/10.1007/s11837-018-2837-9. ISSN 15431851.